Published in final edited form as:

NMR Biomed. 2023 June ; 36(6): e4711. doi:10.1002/nbm.4711.

Detection of tissue pH with quantitative chemical exchange saturation transfer MRI

Takahiro Igarashi[1,#], **Hahnsung Kim**[2,3], **Phillip Zhe Sun**[1,2,3,*]

[1]Athinoula A. Martinos Center for Biomedical Imaging, Massachusetts General Hospital, Harvard Medical School, Charlestown, MA

[2]Department of Radiology and Imaging Sciences, Emory University School of Medicine, Atlanta, GA

[3]Yerkes Imaging Center, Yerkes National Primate Research Center, Emory University, Atlanta, GA

Abstract

Chemical exchange saturation transfer (CEST) MRI has emerged as a novel means for sensitive detection of dilute labile protons and chemical exchange rates. By sensitizing to pH-dependent chemical exchange, CEST MRI has shown promising results in monitoring tissue statuses such as pH changes in disorders like acute stroke, tumor, and acute kidney injury. This article briefly reviews the basic principles for CEST imaging and quantitative measures, from the simplistic asymmetry analysis to multipool Lorentzian decoupling and quasi-steady-state (QUASS) reconstruction. In particular, the advantages and limitations of commonly used quantitative approaches for CEST applications are discussed.

Graphical Abstract

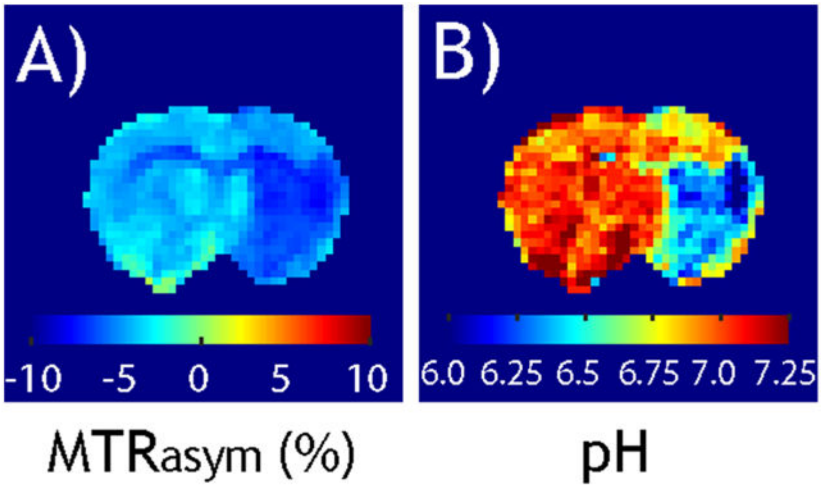

---

[*]Corresponding Author: Phillip Zhe Sun, Ph.D., Department of Radiology and Imaging Sciences, Emory University School of Medicine, 954 Gatewood Road NE, Atlanta, GA 30329, Phone: (404) 727-7786; (404) 712-1667, pzhesun@emory.edu.

[#]Current Address
Department of Neurological Surgery, Nihon University School of Medicine, Tokyo, Japan

Transition from pH-weighted MTR_{asym} image (A) and tissue pH map reconstructed from pH-specific MRAPT analysis (B).

Keywords

Acute stroke; Amide proton transfer (APT); Chemical exchange saturation transfer (CEST); pH; pH-weighted; Tumor

Introduction

pH is a physiological index tightly regulated in healthy tissue (1,2). A notable pH change often signals altered tissue states, such as those following acute ischemia (3-8) and the development of cancer (9-15). For example, tissue acidosis is associated with anaerobic glycolysis following acute stroke (16-19). pH drop compromises essential ATP-dependent functions, often leading to cell death and ultimately tissue infarction (20-24). In the case of cancers, excessive amounts of lactate are produced, disrupting pH homeostasis, a hallmark of the Warburg effect (25-27). It has been recognized that pH change profoundly affects tumor growth and metastasis (28). As such, pH measurement may provide novel insights into tissue microenvironment and response to therapy, and potentially facilitate the development of new therapeutics.

pH measurement in vivo, however, is not straightforward because common strategies such as pH immunohistology, fluorescence microscopy, or phosphorus magnetic resonance approaches are either invasive (29-33), of limited penetration depth (34,35), or insensitive (36-38). To address such an unmet biomedical need, Balaban and co-workers introduced chemical exchange saturation transfer (CEST) MRI as a new sensitive means of imaging pH and dilute labile protons (39-42), laying the groundwork for CEST MRI research over the following two decades (43-48). The proton exchange between macromolecule backbone labile (e.g., amide, amine, and guanidyl groups) and solvent protons is highly pH-dependent, often presenting as a U-shaped curve for acid-base catalysis and conferring pH sensitivity to CEST MRI (49). The typical peptide proton exchange ranges from the low teens for amide protons to a few thousand for amine and hydroxyl groups, depending on the molecule size and exchangeable groups (50). When the exchange rate between two proton groups is much lower than their chemical shift difference, it is considered slow exchange (51). The slow exchange process is particularly amenable to CEST MRI because the saturation of labile proton can be isolated from the solvent proton signal, resulting in efficient saturation of labile protons and their transfer to the bulk water for induction of the CEST effect. CEST MRI has been increasingly adopted to measure certain key metabolites such as glutamate, glutamine, creatine, ensemble amide protons from mobile proteins and peptides, and intracellular pH (52-59). Although the endogenous CEST signal has been attributed mainly to the intracellular compartment, the development of exogenous CEST contrast agents enables imaging of the extracellular space, complementing the endogenous intracellular imaging. Therefore, it is foreseeable that pH imaging (intracellular and extracellular) is beneficial, particularly in tumor imaging (60,61).

CEST MRI experiments are complex, highly dependent on the scan conditions and post-processing analysis. Despite the substantial progress the field has achieved in the theoretical framework of the CEST MRI quantification, many different CEST indices have been adopted. For example, the simplistic magnetization transfer ratio asymmetry analysis has been commonly used despite its limitation in the presence of multiple exchangeable groups. On the other hand, the development of Lorentzian and model-based fittings can account for multiple partially overlapping CEST effects. Such analyses are time-consuming, however, and often limited by image sensitivity. Where quantitative analyses such as omega plots and ratiometric approaches are feasible in contrast agent-based applications, their in vivo implementation requires thorough optimization and Lorentzian fitting. We aim to provide a concise overview of commonly used CEST MRI quantification methods and discuss their advantages and limitations.

Quantitative Description of CEST MRI Signal

2-pool CEST solution

CEST MRI measurement depends not only on the concentration and exchange properties of labile protons, but also on experimental conditions and relaxation constants (62-64). The CEST MRI phenomenon can be mathematically described using Bloch-McConnell equations (65-67). However, the numerical nature of the Bloch-McConnell equations provides limited insights into the contrast mechanism. To address this, analytical CEST MRI solutions, albeit only approximations, have been developed. For a classical 2-pool exchange model under the condition of long RF saturation, the equilibrium CEST effect can be approximated by (68-70)

$$CESTR \approx \frac{f_r \cdot k_{sw}}{R_{1w}} \cdot \alpha \cdot (1-\sigma) \tag{1}$$

in which CESTR stands for CEST ratio, k_{sw} and f_r are the labile proton exchange rate and fraction ratio, and R_{1w} is the bulk water longitudinal relaxation rate, with α and σ being two experimental factors. Briefly, α is the labeling coefficient that accounts for the saturation efficiency of labile protons (71). σ is the RF spillover factor, which describes the concomitant direct RF saturation of the bulk water signal that competes with the CEST-specific MRI effect (72). The product of the experimental factors needs to be optimized to maximize the measurable CEST MRI effect. Overall, the 2-pool CEST MRI solution (Eq. 1) depicts a balance between bulk water signal decrease caused by its exchange with saturated labile protons and its signal recovery due to its T_1 relaxation.

Spinlock-based multipool CEST solution

Although the multipool CEST MRI phenomenon can be modeled by extending Bloch-McConnell equations, it quickly becomes tedious for more than three labile proton groups (73,74). The multipool CEST asymmetry effect can be described by superimposing multiple 2-pool models, provided that each labile proton group is sufficiently dilute so the interaction term can be accounted for (75). Fortunately, the introduction of the spinlock theorem to the CEST MRI field enormously simplified the modeling of the CEST effect (76-78). Briefly, the Z-spectral intensity is described by

$$\frac{S_{sat}}{S_0} = e^{-R_{1\rho} \cdot Ts} + \frac{R_{1w}}{R_{1\rho}} cos^2\theta \cdot \left(1 - e^{-R_{1\rho} \cdot Ts}\right) \tag{2}$$

where Ts is the RF saturation time, $R_{1\rho}$ is the spinlock relaxation rate under the RF saturation, being $R_{1\rho} = R_{1w}cos^2\theta + R_{2w}sin^2\theta + \sum_{i=1}^{N} R_{ex}^i$, with R_{ex}^i being the ith pool CEST effect, $\theta = tan^{-1}(\omega_1 / \Delta\omega)$, in which ω_1 and $\Delta\omega$ are the RF saturation amplitude and offset, in radian, respectively. The spinlock formula has been extended to describe magnetization transfer (MT) ratio asymmetry (MTR_{asym}), a commonly used metric to quantify CEST effects (79), and the pulse RF saturation scheme (80-82).

Generalized CEST solution

It is worth mentioning that Eq. 2 is accurate under the condition of complete relaxation recovery, which may not be fulfilled when the repetition time is shortened to reduce the overall scan time. Jiang et al. extended the CEST solution to incorporate experimental parameters such as flip angle (FA), relaxation delay (Td) and Ts (83). The Z-spectral intensity for CEST MRI with gradient-echo (GE) readout can be shown as

$$\frac{S_{sat}(R_{1\rho}(B_1, \Delta\omega), TR, FA, Ts)}{S_0(TR, FA)} = \frac{\dfrac{\left(1 - e^{-Td / T_{1w}}\right) \cdot e^{-R_{1\rho}(B_1, \Delta\omega) \cdot Ts} + \dfrac{R_{1w}cos^2\theta}{R_{1\rho}(B_1, \Delta\omega)} \cdot \left(1 - e^{-R_{1\rho}(B_1, \Delta\omega) \cdot Ts}\right)}{1 - cos(FA) \cdot e^{-Td / T_{1w}} \cdot e^{-R_{1\rho} \cdot Ts}}}{\left(1 - e^{-TR / T_{1w}}\right) / \left(1 - cos(FA) \cdot e^{-TR / T_{1w}}\right)} \tag{3}$$

This generalized formula facilitates scan optimization and quantification.

Recently, Sun proposed quasi-steady-state (QUASS) CEST reconstruction, which solves the equilibrium $R_{1\rho}$ (i.e., $R_{1\rho}^{QUASS}(B_1, \Delta\omega)$) from the experimental CEST measurement under the condition of finite saturation time and relaxation delay (84). The equilibrium CEST effect can be reconstructed as

$$\left(\frac{S_{sat}}{S_0}\right)^{QUASS} = \frac{R_{1w}}{R_{1\rho}^{QUASS}(B_1, \Delta\omega)} cos^2\theta \tag{4}$$

One of the advantages of QUASS CEST MRI is that the CEST scans can be expedited without resorting to long scan duration, while the magnitude of the CEST effect can be recovered from QUASS reconstruction.

Quantitative CEST MRI Measurements

MTR asymmetry

The commonly used MTR_{asym} takes the difference between the signals with RF saturation applied on the reference frequency (−Δω) and the labile frequency (Δω), symmetric around the bulk water resonance

$$MTR_{asym} = \frac{S_{sat}(-\Delta\omega) - S_{sat}(\Delta\omega)}{S_0} \tag{5}$$

The asymmetry calculation corrects RF spillover and, to a lesser degree, the semisolid MT effects (47). Zhou et al. determined the amide proton exchange rate from water exchange spectroscopy and calibrated it against pH determined by phosphorus (31P) spectroscopy. The calibration was further applied to map $\mathrm{MTR}_{\mathrm{asym}}$ for absolute tissue pH (85). Due to the slow amide exchange rate, ischemia-induced $\mathrm{MTR}_{\mathrm{asym}}$ contrast peaks with a relatively mild RF saturation amplitude (86). In addition to APT, there are multiple partially overlapping exchangeable groups such as amine and guanidyl CEST MRI effects, suggesting the possibility of combining them and enhancing the pH contrast. For example, Jin et al. took the signal difference between 3.6 ppm (amide) and 2 ppm (guanidyl) as a new pH-weighted measure (87). Because of their exchange rate difference, a small pH change causes their signals to vary in an opposite direction, resulting in a larger signal change ($\mathrm{pH}_{\mathrm{enh}}$). Jin et al. showed that whereas APT-weighted (APTw) at 3.6 ppm indicated a small signal drop (Fig. 1a) following tissue acidosis induced by CO_2 challenge, $\mathrm{pH}_{\mathrm{enh}}$ detects a more substantive signal increase (Fig. 1b). To rule out that the observed $\mathrm{pH}_{\mathrm{enh}}$ is not due to perfusion change, the experiments were repeated with an O_2 challenge, which induces hemodynamic changes but not pH (Fig. 1c). Fig. 1d shows the average time course of APTw and $\mathrm{pH}_{\mathrm{enh}}$ obtained from the cortex, with the peak signal change in $\mathrm{pH}_{\mathrm{enh}}$ much stronger than APTw. It is important to note that exchange rates of amide, amine, and guanidyl groups with respect to pH differ substantially, allowing variant pH imaging methodologies. For example, $\mathrm{MTR}_{\mathrm{asym}}$ at 3 ppm (amine) obtained under a high RF saturation amplitude has been applied to map tumor pH (88), which may serve as a potential early biomarker for recurrent glioblastoma (89,90). pH-weighted imaging has also been correlated with tumor hypervascularity (91).

It is worth noting that an index similar to $\mathrm{MTR}_{\mathrm{asym}}$ is the apparent relaxation exchange (AREX), which utilizes inverse normalization to linearize the CEST calculation (77). Inverse asymmetry calculation also allows for T_1 normalization, which is not easily applicable when using $\mathrm{MTR}_{\mathrm{asym}}$. Specifically, we have

$$AREX = R_{1w} \cdot \left(\frac{S_0}{S_{sat}(+\Delta\omega)} - \frac{S_0}{S_{sat}(\Delta\omega)}\right) \tag{6}$$

In the presence of multiple CEST effects that are partially overlapping or bilaterally around the bulk water resonance, both $\mathrm{MTR}_{\mathrm{asym}}$ and AREX reflect a mixture of contrasts. The asymmetry analysis is simple to use, yet prone to confounding contributions from multipool CEST and changes in relaxation and asymmetric semisolid macromolecular effects. As a result, pH-weighted $\mathrm{MTR}_{\mathrm{asym}}$ has been demonstrated in acute stroke imaging without substantial changes in relaxation and semisolid MT effects.

Direct Saturation-Corrected (DISC) CEST

Instead of the asymmetry calculation, Sun et al. (92) and Jin et al. (93) proposed interpolating signals at two neighboring offsets around the labile proton offset as the baseline to isolate APT and nuclear Overhauser enhancement (NOE) effects. However, linear baseline interpolation is simplistic because the direct RF saturation is nonlinear concerning the RF offset. Zhou et al. proposed a direct saturation-correction (DISC) algorithm to correct the direct RF saturation based on relaxation images. Furthermore, because the MT effect has a broad spectrum, it can be described as a linear baseline (94). The DISC-CEST method allows for using asymmetric boundary offsets

$$APTR_{DISC}(\Delta\omega_i) = \frac{\delta_1 \cdot \Delta Z(\Delta\omega_i + \delta_2) + \delta_2 \cdot \Delta Z(\Delta\omega_i - \delta_1)}{\delta_1 + \delta_2} - \Delta Z(\Delta\omega_i) \tag{7}$$

in which the upfield and downfield boundaries are $\Delta\omega_i - \delta_1$ and $\Delta\omega_i + \delta_2$, respectively. In addition, ΔZ is the Z-spectral intensity difference between the experimental measurement (multipool) and bulk tissue water signal due to direct RF saturation alone (one-pool). The DISC approach has been extended to 3T, which is advantageous over the simplistic linear estimation of the baseline (95). The limitation of the DISC analysis is that it provides a mixed measurement in the presence of multiple overlapping CEST effects. Therefore, weak RF saturation is often preferred to isolate the CEST effect (slow chemical exchange) of interest.

Magnetization transfer and relaxation normalized APT (MRAPT) analysis

Although MTR_{asym} at 3.5 ppm has been associated with tissue acidification in acute stroke (96), it includes not only the APT effect but also T_1, NOE effect at −3.5 ppm, and slightly asymmetric semisolid MT contributions (97-103). Studies from Jin et al. and Zhou et al. showed little NOE signal change in hyperacute stroke (93,104). However, both APT and NOE signal changes have been observed in acute stroke (105,106). Recently, Wu et al. traced the apparent NOE signal change during the acute stroke to a small T_1 change. Specifically, there have been reports of a non-negligible T_1 increase in the acute ischemic lesion (107,108). The exchange spectrum (R_{ex}) was calculated by subtracting the water spinlock relaxation rate from the experimental measurement. Whereas Z-spectra showed comparable APT and NOE signal changes, the CEST-specific exchange spectra revealed that APT signal change dominates that of NOE.

The MRAPT analysis has been developed to improve pH specificity in the pH-weighted MTR_{asym} image (109). This is built on the observations that 1) there is little pH difference in the intact white matter and gray matter (110); 2) pH effect in MT contrast is negligible (111); and 3) APT signal change dominates NOE's in acute ischemia (93,107). The background homogenization provides a straightforward approach to model and correct non-pH signals in the routine MTR_{asym} image. Specifically, we have

$$\Delta MRAPTR = R_{1w} \cdot MTR_{asym} - F(R_{1w}, MMTR) \tag{8}$$

where the mean MTR at ±3.5 ppm is denoted as MMTR. pH-specific ΔMRAPTR has been calibrated against pH determined from lactate MR spectroscopy (108,112), with the correlation between ΔMRAPTR and pH substantially improved over that of MTR_{asym}. Specifically, Fig. 2a shows that pH-specific ΔMRAPTR from the diffusion lesion highly correlates with tissue pH. Fig. 2b shows the pH-weighted MTR_{asym} image, while Fig.

2c shows the pH-specific ΔMRAPTR image. Fig. 2d converts the ΔMRAPTR image to absolute tissue pH. Note that pH captured not only the severe pH drop in the ischemic core, but also mild acidic tissue in the primary motor cortex. It is also worth pointing out that the development of pH-specific MRI makes fast B_0 inhomogeneity correction feasible by incorporating the field inhomogeneity into the MRAPT regression model (113). Also, the MRAPT analysis can be generalized to APT MRI with pulsed-RF saturation (114) and different RF saturation amplitudes (115). Although the MRAPT analysis is simple to implement and highly pH specific, it assumes little concomitant MT change, so regression established from the intact tissue applies to the diseased tissue. The approach is limited to well-defined applications such as acute stroke imaging, where MT change is minimal.

Quantitative CEST (qCEST) analysis

There has been tremendous interest in solving the labile proton ratio and exchange rate beyond the CEST-weighted images (116,117). McMahon et al. quantified the exchange rate using either saturation power or time dependence (QUESP and QUEST) by fitting the CEST signal as a function of RF saturation amplitudes and durations (118). Randtke et al. proposed Hanes-Woolf linear QUESP and inverse QUEST to improve the quantification (119,120). Sun extended the QUEST algorithm with ratiometric analysis (QUESTRA) to enhance the quantification accuracy (121). This approach addresses the issue that the rate at which the CEST effect approaches its equilibrium state is not governed by R_{1w} but by $R_{1\rho}$. Hence, using the reference signal provides a simple normalization strategy to account for the spinlock relaxation without the need to measure it. These algorithms were extended to describe non-equilibrium initial and weak labeling conditions (122). Although a quantitative CEST solution determines labile proton exchange rate and concentration of the underlying CEST system, it has been mainly limited to applications using exogenous CEST contrast agents. The multipool contribution needs to be isolated for in vivo applications, so the same labile group is measured under different conditions (e.g., B_1). However, this task is not trivial because the typical endogenous CEST effect is a few percent; hence, of very limited sensitivity.

It has been noted that RF amplitude provides a unique dimension for quantitative CEST analysis (123). Dixon et al. proposed an omega plot to solve the exchange rate without a priori knowledge of the labile proton ratio in paramagnetic CEST (PARACEST) MRI (124). In short, the plot of the CEST effect versus inverse RF power level is linear, with the x-intercept providing a direct measurement of the exchange rate. It has been shown that with the correction of the RF spillover effect, the omega plot could be extended to describe diamagnetic CEST (DIACEST) agents (125,126). Also, quantitative CEST MRI has been preliminarily applied to study muscle and brain tissue (127,128).

QUASS CEST MRI

The finite relaxation delay and saturation time can be accounted for using the recent QUASS algorithm, which reconstructs the equilibrium CEST effect from experimental measurement. Fig. 3 shows the routine and QUASS MTR_{asym} images from a dual pH creatine phantom using Td/Ts ranging from 1.5 to 7.5 s. Fig. 3a shows that the routine MTR_{asym} intensity increases with Td and Ts as it approaches the equilibrium CEST state. Figs. 3b and 3c show the corresponding CEST Z- and asymmetry spectra, respectively, revealing large variations as a function of Ts and Td, as expected. In comparison, the QUASS Z- (Fig. 3d) and asymmetry- (Fig. 3e) spectra overlap with each other, revealing consistent pH-specific CEST MRI contrast (Fig. 3f). The data shows that the QUASS algorithm can unify CEST scans obtained under different conditions. Also, it has been shown that the ratiometric analysis based on the QUASS solution provides improved quantification of the labile proton fraction ratio and exchange rate over those with apparent measurement (129). In addition, using the inverse Z-spectrum normalization combined with QUASS reconstruction enables proper T_1 correction (130). Furthermore, the QUASS processing has been recently demonstrated in fast multislice CEST imaging at 3T (131) and brain tumor applications (132,133). Although the QUASS algorithm enables equilibrium CEST quantification, it requires parametric T_1 mapping (134), which could lengthen the total scan time.

Lorentzian fitting

The Lorentzian fitting has been developed to describe CEST measurement in the presence of multiple labile proton groups. Briefly, the normalized Z-signal change can be described by

$$1-\frac{S_{sat}}{S_0}\approx\frac{\sum_{i=1}^{N} f_r^i k_{sw}^i\cdot\alpha^i}{R_{1\rho}}\approx\sum_{i=1}^{N}\frac{f_r^i k_{sw}^i}{R_{1w}}\cdot\alpha^i \tag{9}$$

in which the superscript i represents the i^{th} labile proton group. The labeling coefficient can be approximated as a Lorentzian function. The choice of the number of labile pools depends on the field strength, RF saturation scheme, Z-spectral sampling density, and SNR. For example, multipool Lorentzian models including water (0 ppm), semisolid macromolecular MT (−2 ppm), amide (3.5 ppm), amine (2.75 ppm), guanidinium (2 ppm), and NOE effects at 1.6 ppm and 3.5 ppm upfield from water have been deployed to describe brain CEST effects (104,135-137). Although the accuracy improves with the number of CEST pools, the nonlinear multiparameter fitting is subject to substantial errors when the spectral resolution and SNR are insufficient. To enhance the robustness of fitting, Zhou et al. proposed the image downsampling expedited adaptive least-squares (IDEAL) algorithm to regularize the fitting against noise (138). Nevertheless, for applications at low fields such as 3T, the Z-spectrum has a relatively coarse spectral resolution. Therefore, models of 3 or 4 exchangeable pools are often chosen to minimize the risk of overfitting (139,140). To address the pronounced MT effect, Heo et al. proposed fitting and extrapolating semisolid magnetization transfer reference (EMR) to remove it from Z-spectra (141,142). The EMR approach has been applied to isolate APT from NOE effects in acute stroke patients and showed improved lesion depiction (105).

Several factors need to be considered when deploying the multipool Lorentzian fitting. First, the Lorentzian fitting is valid when the saturation time is sufficiently long: The transient terms could introduce an asymmetric baseline because the spinlock relaxation rate increases when the RF saturation approaches the bulk water resonance (143). Second, in the presence of notable changes in relaxation rates, which is not uncommon in diseased tissues, the bulk water spinlock relaxation term will induce a symmetric baseline shift. Such a baseline change needs to be considered when assigning the origin of the CEST contrast.

Third, although T_1 normalization improves the measurement of the labile proton ratio and exchange rate (144-146), how to properly account for the T_1 effect in CEST imaging in vivo (147,148) is controversial. One particular limitation of Lorentzian fitting is that it requires a reasonably densely sampled Z-spectrum; therefore, it could be time-consuming.

Model-based fitting

The Bloch-McConnell equations have been extended to describe the multipool CEST effect. For example, Sun et al. applied 5-pool models to determine exchange properties of iopamidol (74). However, multipool fitting requires many free parameters and is at the risk of overfitting. Chappell et al. introduced the Bayesian model to regularize the fitting (149). Specifically, Ray et al. demonstrated that Bayesian model-based analysis (BayCEST) with relaxation compensation provides robust pH-sensitive measurement (150). BayCEST was further shown in acute stroke patients to be advantageous over MTR_{asym} in defining the ischemic lesion (151). Msayib et al. compared different indices in acute stroke patients, including MTR_{asym}, AREX, and APT* with local linear baseline assumptions, post-acquisition Lorentzian difference analysis, and APTR* from 3-pool and 4-pool Bayesian models (152). Fig. 4 shows that the 3-pool Bayesian model exhibits the lowest spatial variability, yet captures pH drop in the ischemic lesion. Foo et al. also concluded that the model-based fitting is advantageous when SNR is inadequate (153). It is interesting to point out that using the BayCEST approach, Ray et al. concluded that 2/3 of APT contrast originates from changes in protein concentration, while the remaining 1/3 comes from changes in tumor pH (154). Whereas the model-based fitting approach is robust, it requires a reasonably densely sampled Z-spectrum, which could be computation-intensive and time-consuming.

Ratiometric analysis

The original ratiometric pH imaging requires the CEST agent to have at least two exchangeable groups of different chemical shifts and exchange properties, so their ratio depends only on the exchange rate and, hence, pH (42). Aime et al. reported iopamidol, a CT contrast agent, as a new CEST MRI contrast (155-157). The iopamidol ratiometric analysis depends only on pH, not on T_1 and CEST agent concentration. Due to its FDA-approved status, iopamidol is highly translational for in vivo CEST imaging (158,159). Longo et al. showed that pH is a sensitive biomarker of early acute ischemic injury before creatinine level change (160). Pavuluri showed that in addition to pH, iopamidol MRI could quantify renal perfusion status (161).

Beyond iopamidol, several iodinated contrast agents have been explored for pH imaging, including Iopromide (162) and Imidazole (163). Furthermore, the ratiometric CEST MRI has been extended to CEST agents of a single liable proton group. Specifically, RF power-based ratiometric takes the ratio of CEST measurements performed under different B_1 saturation amplitudes instead of two different chemical shifts, and was demonstrated using iobitridol (164-166). Wu et al. further generalized the ratiometric pH imaging by mixing CEST effects at different chemical shifts and RF saturation levels (167). Fig. 5 shows the generalized ratiometric renal pH imaging in a rodent kidney. The iopamidol CEST effects at 4.3 ppm and 5.5 ppm were isolated using Lorentzian fitting with RF amplitudes of 1 and 2 μT, respectively. Absolute renal pH can be mapped using the modified ratiometric pH imaging. The generalized pH imaging is versatile for CEST applications at non-high magnetic fields, where the CEST effects might partially overlap, decreasing the dynamic range of routine ratiometric analysis. Similarly, Zu et al. used the RF saturation pulse flip angle as an alternative to measuring the chemical exchange rate (168). The ratiometric pH imaging approach has also been explored for endogenous pH mapping. McVicar et al. demonstrated the endogenous ratiometric MRI of amine and amide concentration-independent detection (AACID) for mapping ischemic tissue pH (169). However, endogenous ratiometric pH imaging assumes that the concentration of different labile groups is relatively stable, which needs to be validated independently under pathological conditions.

The ratiometric MRI approach has also been applied in vivo to map pH in cancerous tissues. Chen demonstrated dual RF power ratiometric pH imaging using Ioversol in mouse breast cancer (170). Recently, Tang et al. translated Ioversol pH MRI to examine hepatic tumor patients at 3T. Fig. 6a shows a patient with hepatic hemangioma, with its corresponding pH map (Fig. 6b). Note that pH was consistent with the surrounding liver tissue, confirming benign hemangioma. Fig. 6c shows a patient with hepatic carcinoma, with its pH in Fig. 6d. Its pH is significantly lower than the normal tissue. Indeed, pH in hepatic carcinoma was acidic (6.66 ± 0.19), while the extracellular pH was 7.34 ± 0.09 in hemangioma, demonstrating pH MRI as a differential diagnostic imaging methodology (171). Increasing data have documented that tumor extracellular pH is lower in faster-growing tumors, serving as a surrogate marker for differentiating benign and malignant tumors and early response to treatment.

It is helpful to mention that CEST pH MRI has certain advantages over the relaxation-based pH imaging approach. For example, although the relaxivity of macromolecular Gd complexes can be extracellular pH-responsive (172), it requires a double-contrast injection approach, sequential or concurrent, to determine the contrast concentration, which is cumbersome (173-175). Another notable extracellular pH imaging approach is biosensor imaging of redundant deviation in shifts (BIRDS), which utilizes pH-responsive chemical shifts to measure pH (176-178). However, its major limitation is that the contrast agent has very short T_1 and T_2 relaxation times, requiring customized imaging sequences. In comparison, pH CEST agents, particularly FDA-approved iodinated-based ones, allow concentration-independent pH imaging and are highly translational. Nevertheless, exogenous CEST agents-based pH imaging requires the administration of contrast agents at relatively high concentrations, mostly appliable in tumor and renal imaging applications.

Practical Considerations of CEST MRI Experiments

It has been well recognized that experimental parameters such as the RF saturation scheme (RF saturation pulse shape, amplitude, and duration), repetition time, and flip angle could profoundly impact the CEST MRI measurement. Therefore, the CEST MRI needs to be carefully optimized to improve its sensitivity and specificity.

Pulse sequence

The most straightforward implementation of the CEST MRI pulse sequence includes a relaxation delay, during which magnetizations recover toward their thermal equilibrium states, followed by a continuous wave (CW) RF irradiation to induce the CEST effect, during which the bulk water signal approaches its CEST equilibrium state following the spinlock relaxation rate. The sequence often concludes with a fast image readout such as echo planar imaging (EPI) or fast spin echo (FSE) readout (179). Although the CW saturation scheme is simple to implement and model mathematically, the pulse RF saturation scheme has been chosen due to the RF duty cycle, specific absorption rate, and hardware limitation (180-182). In addition, the flip angle has been explored as a novel means for isolating the amide CEST effect from the baseline (183,184). Fortunately, CW or pseudo-CW (90% or higher RF duty cycle) RF saturation has been recently demonstrated in mainstream MRI systems, including General Electric, Philips, and Siemens scanners. Although single slice readout was adopted in early clinical CEST imaging, recent CEST development includes substantially improved spatial coverage, including fast multislice (185-187) and 3D readout (141,188-190). Demetriou et al. recently provided a comprehensive review of CEST MRI pulse sequences (191).

Correction of field inhomogeneity in CEST MRI measurement

Field inhomogeneity is not uncommon in MRI experiments, particularly in areas of the tissue air interface. Because the field inhomogeneity directly impacts the saturation of labile protons and the asymmetry analysis, CEST measurement is very prone to field inhomogeneity. The B_0 inhomogeneity on MTR_{asym} can be modeled as a baseline shift due to direct RF saturation and a Lorentzian-shaped modulation of the labeling coefficient (192). For in vivo applications, the water saturation shift reference (WASSR) approach has been widely used to correct the Z-spectrum from field inhomogeneity (193-195). More recently, deep learning has been applied to provide fast correction of field inhomogeneity without Z-spectrum (196). It is worth pointing out that the routine field inhomogeneity correction algorithms assume intravoxel homogeneity. However, due to the relatively coarse spatial resolution of CEST MRI, it is unavoidable to have inhomogeneity within a single voxel. To address this, an intravoxel inhomogeneity correction (CIVIC) post-processing was developed (197). It describes the experimental CEST spectrum (Z_{app}) as a convolution of the ideal CEST spectrum (Z_{orig}) and a point spread function (PSF) that characterizes the intravoxel inhomogeneity distribution (i.e., $F(\Delta B_0)$), as

$$Z_{app} = Z_{orig} \circledast F(\Delta B_0) \tag{10}$$

Using a high-resolution field map, Z_{orig} can be reconstructed, which complements the routine voxel-based field inhomogeneity correction. In addition, although B_1 inhomogeneity has been considered relatively mild at typical field strengths, fast B_1 mapping and correction have been established (198).

Optimization of CEST sensitivity efficiency

Because the typical endogenous CEST effect is only a few percent, optimization of CEST scans is necessary to improve its detection. Initial work was dedicated to optimizing the RF saturation amplitude, with the goal of inducing sufficient labile proton saturation without an excessive spillover effect on the bulk water signal (64). In addition to the magnitude of the CEST MRI effect, its signal-to-noise ratio per unit time (SNR efficiency) serves as an alternative parameter to optimize (199) because the CEST MRI effect increases monotonically with the RF saturation time, yet the incremental gain over an excessively long saturation time becomes marginal. Thus, the repetition time needs to be considered to balance the magnitude and scan time. For an illustrative 2-pool system, the SNR efficiency has been derived as

$$SNR_{put} \propto \frac{CESTR}{\sqrt{TR} \cdot \sqrt{2 + CESTR^2}} \cdot SNR_{S_0} \tag{11}$$

where SNR_{S_0} is the control image SNR, which depends on the flip angle, repetition time, and echo time. The derivation of the full analytical solution makes it feasible to simulate and optimize multiple parameters simultaneously before experimental validation (83). However, the optimization strategy based on the magnitude and SNR efficiency of CEST MRI measurement could contradict each other. Whereas the magnitude of the CEST MRI effect is higher when using a small flip angle, the CEST MRI SNR efficiency peaks when using flip angles between 60 to 75 degrees. The ultimate optimization depends on the purpose of the experiments. Fortunately, the QUASS algorithm allows for sensitivity-based experimental optimization with little loss in the quantification accuracy.

The scan time can be reduced by sampling fewer frequency offsets. For example, sampling multiple offsets only around ±3.5 ppm expedites $\mathrm{MTR}_{\mathrm{asym}}$ measurement, circumventing time-consuming Z-spectral acquisition (200). For the Z-spectral imaging, it has been demonstrated that an uneven sampling scheme may provide similar results as the fully sampled Z-spectrum, particularly at 3T (201,202).

Conclusion

Steady progress has been achieved in CEST imaging, with increased specificity and sensitivity to pH. The technical advancement enables emerging applications in disorders such as acute stroke and cancer. Further development of robust CEST analysis and post-processing algorithms will expedite its adoption in the clinical setting, facilitating the transition from CEST-weighted imaging to quantitative maps of tissue pH and metabolites.

Abbreviations

APT	Amide proton transfer
CEST	Chemical exchange saturation transfer
CESTR	CEST ratio

CNR	Contrast to noise ratio
ΔMRAPTR	Delta MRAPT ratio
MT	Magnetization transfer
MMTR	Mean magnetization transfer ratio
MTR	Magnetization transfer ratio
MTR_{asym}	MTR asymmetry
MRAPT	MT and relaxation normalization APT
NOE	Nuclear overhauser enhancement
pHw	pH-weighted
QUAS	Quasi-steady-state
rCNR	Relative CNR
rCESTR	ratiometric CESTR
ΔMRAPTR	Delta MRAPT ratio

References

1. Petroff OA, Prichard JW, Behar KL, Alger JR, den Hollander JA, Shulman RG. Cerebral intracellular pH by 31P nuclear magnetic resonance spectroscopy. Neurology 1985;35(6):781–788. [PubMed: 4000479]
2. Chesler M. Regulation and modulation of pH in the brain. Physiol Rev 2003;83(4):1183–1221. [PubMed: 14506304]
3. Tomlinson FH, Anderson RE, Meyer FB. Acidic foci within the ischemic penumbra of the New Zealand white rabbit. Stroke 1993;24(12):2030–2039; discussion 2040. [PubMed: 8248985]
4. Hossmann KA. Pathophysiology and therapy of experimental stroke. Cellular and molecular neurobiology 2006;26(7-8):1057–1083. [PubMed: 16710759]
5. Katsura K, Ekholm A, Asplund B, Siesjo BK. Extracellular pH in the brain during ischemia: relationship to the severity of lactic acidosis. J Cereb Blood Flow Metab 1991;11(4):597–599. [PubMed: 1904880]
6. Siesjo BK. Pathophysiology and treatment of focal cerebral ischemia: Part I: Pathophysiology. J Neurosurg 1992;77(2):169–184. [PubMed: 1625004]
7. Zhou J, van Zijl PC. Defining an Acidosis-Based Ischemic Penumbra from pH-Weighted MRI. Transl Stroke Res 2011;3(1):76–83. [PubMed: 22408691]
8. Haris M, Singh A, Cai K, Kogan F, McGarvey J, Debrosse C, Zsido GA, Witschey WR, Koomalsingh K, Pilla JJ, Chirinos JA, Ferrari VA, Gorman JH, Hariharan H, Gorman RC, Reddy R. A technique for in vivo mapping of myocardial creatine kinase metabolism. Nat Med 2014;20(2):209–214. [PubMed: 24412924]
9. Hanahan D, Weinberg RA. Hallmarks of cancer: the next generation. Cell 2011;144(5):646–674. [PubMed: 21376230]
10. White KA, Grillo-Hill BK, Barber DL. Cancer cell behaviors mediated by dysregulated pH dynamics at a glance. J Cell Sci 2017;130(4):663–669. [PubMed: 28202602]
11. Zhang X, Lin Y, Gillies RJ. Tumor pH and its measurement. J Nucl Med 2010;51(8):1167–1170. [PubMed: 20660380]

12. Gillies RJ, Raghunand N, Garcia-Martin ML, Gatenby RA. pH imaging. A review of pH measurement methods and applications in cancers. IEEE Eng Med Biol Mag 2004;23(5):57–64.
13. Sagiyama K, Mashimo T, Togao O, Vemireddy V, Hatanpaa KJ, Maher EA, Mickey BE, Pan E, Sherry AD, Bachoo RM, Takahashi M. In vivo chemical exchange saturation transfer imaging allows early detection of a therapeutic response in glioblastoma. Proc Natl Acad Sci U S A 2014;111(12):4542–4547. [PubMed: 24616497]
14. Walker-Samuel S, Ramasawmy R, Torrealdea F, Rega M, Rajkumar V, Johnson SP, Richardson S, Goncalves M, Parkes HG, Arstad E, Thomas DL, Pedley RB, Lythgoe MF, Golay X. In vivo imaging of glucose uptake and metabolism in tumors. Nat Med 2013;19(8):1067–1072. [PubMed: 23832090]
15. Kamimura K, Nakajo M, Yoneyama T, Takumi K, Kumagae Y, Fukukura Y, Yoshiura T. Amide proton transfer imaging of tumors: theory, clinical applications, pitfalls, and future directions. Japanese journal of radiology 2019;37(2):109–116. [PubMed: 30341472]
16. Sun PZ, Zhou J, Sun W, Huang J, van Zijl PC. Detection of the ischemic penumbra using pH-weighted MRI. J Cereb Blood Flow Metab 2007;27(6):1129–1136. [PubMed: 17133226]
17. Astrup J, Siesjo BK, Symon L. Thresholds in cerebral ischemia - the ischemic penumbra. Stroke 1981;12(6):723–725. [PubMed: 6272455]
18. Sako K, Kobatake K, Yamamoto YL, Diksic M. Correlation of local cerebral blood flow, glucose utilization, and tissue pH following a middle cerebral artery occlusion in the rat. Stroke 1985;16(5):828–834. [PubMed: 4049447]
19. Warach S. New imaging strategies for patient selection for thrombolytic and neuroprotective therapies. Neurology 2001;57(5 Suppl 2):S48–52. [PubMed: 11552055]
20. Jeffs GJ, Meloni BP, Bakker AJ, Knuckey NW. The role of the Na(+)/Ca(2+) exchanger (NCX) in neurons following ischaemia. J Clin Neurosci 2007;14(6):507–514. [PubMed: 17430774]
21. Hossmann KA. Viability thresholds and the penumbra of focal ischemia. Ann Neurol 1994;36(4):557–565. [PubMed: 7944288]
22. Xiong ZG, Chu XP, Simon RP. Acid sensing ion channels--novel therapeutic targets for ischemic brain injury. Front Biosci 2007;12:1376–1386. [PubMed: 17127388]
23. Shi Y, Chanana V, Watters JJ, Ferrazzano P, Sun D. Role of sodium/hydrogen exchanger isoform 1 in microglial activation and proinflammatory responses in ischemic brains. J Neurochem 2011;119(1):124–135. [PubMed: 21797866]
24. Simon R, Xiong Z. Acidotoxicity in brain ischaemia. Biochem Soc Trans 2006;34(Pt 6):1356–1361. [PubMed: 17073818]
25. Warburg O. On the origin of cancer cells. Science 1956;123(3191):309–314. [PubMed: 13298683]
26. Vander Heiden MG, Cantley LC, Thompson CB. Understanding the Warburg effect: the metabolic requirements of cell proliferation. Science 2009;324(5930):1029–1033. [PubMed: 19460998]
27. Alfarouk KO. Tumor metabolism, cancer cell transporters, and microenvironmental resistance. J Enzyme Inhib Med Chem 2016;31(6):859–866. [PubMed: 26864256]
28. Thews O, Riemann A. Tumor pH and metastasis: a malignant process beyond hypoxia. Cancer Metastasis Rev 2019;38(1-2):113–129. [PubMed: 30607627]
29. Csiba L, Paschen W, Hossmann KA. A topographic quantitative method for measuring brain tissue pH under physiological and pathophysiological conditions. Brain Res 1983;289(1-2):334–337. [PubMed: 6661650]
30. Mutch WA, Hansen AJ. Extracellular pH changes during spreading depression and cerebral ischemia: mechanisms of brain pH regulation. J Cereb Blood Flow Metab 1984;4(1):17–27. [PubMed: 6693512]
31. LaManna JC. Intracellular pH determination by absorption spectrophotometry of neutral red. Metab Brain Dis 1987;2(3):167–182. [PubMed: 3333173]
32. Tomlinson FH, Anderson RE, Meyer FB. Brain pHi, cerebral blood flow, and NADH fluorescence during severe incomplete global ischemia in rabbits. Stroke 1993;24(3):435–443. [PubMed: 8446980]
33. Regli L, Anderson RE, Meyer FB. Effects of intermittent reperfusion on brain pHi, rCBF, and NADH during rabbit focal cerebral ischemia. Stroke 1995;26(8):1444–1451; discussion 1451-1442. [PubMed: 7631351]

34. Khan T, Soller B, Naghavi M, Casscells W. Tissue pH determination for the detection of metabolically active, inflamed vulnerable plaques using near-infrared spectroscopy: an in-vitro feasibility study. Cardiology 2005;103(1):10–16. [PubMed: 15528895]

35. Kim H, Krishnamurthy LC, Sun PZ. Brain pH Imaging and its Applications. Neuroscience 2021;474:51–62. [PubMed: 33493621]

36. Moon RB, Richards JH. Determination of intracellular pH by 31P magnetic resonance. J Biol Chem 1973;248(20):7276–7278. [PubMed: 4743524]

37. Ren J, Shang T, Sherry AD, Malloy CR. Unveiling a hidden (31) P signal coresonating with extracellular inorganic phosphate by outer-volume-suppression and localized (31) P MRS in the human brain at 7T. Magn Reson Med 2018;80(4):1289–1297. [PubMed: 29427295]

38. Korzowski A, Weinfurtner N, Mueller S, Breitling J, Goerke S, Schlemmer HP, Ladd ME, Paech D, Bachert P. Volumetric mapping of intra- and extracellular pH in the human brain using (31) P MRSI at 7T. Magn Reson Med 2020;84(4):1707–1723. [PubMed: 32237169]

39. Guivel-Scharen V, Sinnwell T, Wolff SD, Balaban RS. Detection of proton chemical exchange between metabolites and water in biological tissues. J Magn Reson 1998;133(1):36–45. [PubMed: 9654466]

40. Dagher AP, Aletras A, Choyke P, Balaban RS. Imaging of urea using chemical exchange-dependent saturation transfer at 1.5T. J Magn Reson Imaging 2000;12:745–748. [PubMed: 11050645]

41. Ward KM, Aletras AH, Balaban RS. A new class of contrast agents for MRI based on proton chemical exchange dependent saturation transfer (CEST). J Magn Reson 2000;143(1):79–87. [PubMed: 10698648]

42. Ward KM, Balaban RS. Determination of pH using water protons and chemical exchange dependent saturation transfer (CEST). Magn Reson Med 2000;44(5):799–802. [PubMed: 11064415]

43. van Zijl PCM, Yadav NN. Chemical exchange saturation transfer (CEST): What is in a name and what isn't? Magnetic resonance in medicine 2011;65(4):927–948. [PubMed: 21337419]

44. Dula AN, Arlinghaus LR, Dortch RD, Dewey BE, Whisenant JG, Ayers GD, Yankeelov TE, Smith SA. Amide proton transfer imaging of the breast at 3 T: establishing reproducibility and possible feasibility assessing chemotherapy response. Magn Reson Med 2013;70(1):216–224. [PubMed: 22907893]

45. Wu Y, Zhang S, Soesbe TC, Yu J, Vinogradov E, Lenkinski RE, Sherry AD. pH imaging of mouse kidneys in vivo using a frequency-dependent paraCEST agent. Magn Reson Med 2016;75(6):2432–2441. [PubMed: 26173637]

46. Jones KM, Pollard AC, Pagel MD. Clinical applications of chemical exchange saturation transfer (CEST) MRI. J Magn Reson Imaging 2018;47(1):11–27. [PubMed: 28792646]

47. Zhou J, Heo HY, Knutsson L, van Zijl PCM, Jiang S. APT-weighted MRI: Techniques, current neuro applications, and challenging issues. J Magn Reson Imaging 2019;50(2):347–364. [PubMed: 30663162]

48. van Zijl PCM, Lam WW, Xu J, Knutsson L, Stanisz GJ. Magnetization Transfer Contrast and Chemical Exchange Saturation Transfer MRI. Features and analysis of the field-dependent saturation spectrum. NeuroImage 2018;168:222–241. [PubMed: 28435103]

49. Englander SW, Downer NW, Teitelbaum H. Hydrogen exchange. Annual review of biochemistry 1972;41:903–924.

50. Zu Z, Vandsburger M, Sun PZ. Chemical Exchange Mapping. In: Seiberlich N, Gulani V, Calamante F, Campbell-Washburn A, Doneva M, Hu HH, Sourbron S, editors. Quantitative Magnetic Resonance Imaging. Volume 1, Advances in Magnetic Resonance Technology and Applications: Academic Press; 2020. p 857–883.

51. Forsen S, Hoffman RA. Study of Moderately Rapid Chemical Exchange Reactions by Means of Nuclear Magnetic Double Resonance. Journal of Chemical Physics 1963;39(11):2892-&.

52. Aime S, Barge A, Delli Castelli D, Fedeli F, Mortillaro A, Nielsen FU, Terreno E. Paramagnetic lanthanide(III) complexes as pH-sensitive chemical exchange saturation transfer (CEST) contrast agents for MRI applications. Magn Reson Med 2002;47(4):639–648. [PubMed: 11948724]

53. Zhang S, Merritt M, Woessner DE, Lenkinski RE, Sherry AD. PARACEST agents: modulating MRI contrast via water proton exchange. Acc Chem Res 2003;36(10):783–790. [PubMed: 14567712]
54. Cai K, Haris M, Singh A, Kogan F, Greenberg JH, Hariharan H, Detre JA, Reddy R. Magnetic resonance imaging of glutamate. Nat Med 2012;18(2):302–306. [PubMed: 22270722]
55. Zaiss M, Kunz P, Goerke S, Radbruch A, Bachert P. MR imaging of protein folding in vitro employing nuclear-Overhauser-mediated saturation transfer. NMR Biomed 2013;26(12):1815–1822. [PubMed: 24115020]
56. Hingorani DV, Randtke EA, Pagel MD. A catalyCEST MRI contrast agent that detects the enzyme-catalyzed creation of a covalent bond. J Am Chem Soc 2013;135(17):6396–6398. [PubMed: 23601132]
57. Huang Y, Coman D, Ali MM, Hyder F. Lanthanide ion (III) complexes of 1,4,7,10-tetraazacyclododecane-1,4,7,10-tetraaminophosphonate for dual biosensing of pH with chemical exchange saturation transfer (CEST) and biosensor imaging of redundant deviation in shifts (BIRDS). Contrast Media Mol Imaging 2015;10(1):51–58. [PubMed: 24801742]
58. Pumphrey AL, Ye S, Yang Z, Simkin J, Gensel JC, Abdel-Latif A, Vandsburger MH. Cardiac Chemical Exchange Saturation Transfer MR Imaging Tracking of Cell Survival or Rejection in Mouse Models of Cell Therapy. Radiology 2017;282(1):131–138. [PubMed: 27420900]
59. Vinogradov E. Imaging molecules. J Magn Reson 2019;306:145–149. [PubMed: 31337563]
60. Anemone A, Consolino L, Arena F, Capozza M, Longo DL. Imaging tumor acidosis: a survey of the available techniques for mapping in vivo tumor pH. Cancer and Metastasis Reviews 2019;38(1):25–49. [PubMed: 30762162]
61. Damaghi M, Wojtkowiak J, Gillies R. pH Sensing and Regulation in Cancer. Frontiers in physiology 2013;4:370. [PubMed: 24381558]
62. Vinogradov E, Sherry AD, Lenkinski RE. CEST: from basic principles to applications, challenges and opportunities. J Magn Reson 2013;229(0):155–172. [PubMed: 23273841]
63. Liu G, Song X, Chan KW, McMahon MT. Nuts and bolts of chemical exchange saturation transfer MRI. NMR Biomed 2013;26(7):810–828. [PubMed: 23303716]
64. Kim J, Wu Y, Guo Y, Zheng H, Sun PZ. A review of optimization and quantification techniques for chemical exchange saturation transfer MRI toward sensitive in vivo imaging. Contrast Media Mol Imaging 2015;10(3):163–178. [PubMed: 25641791]
65. McConnell HM. Reaction Rates by Nuclear Magnetic Resonance. Journal of Chemical Physics 1958;28(3):430–431.
66. Reeves L, Shaw K. Nuclear magnetic resonance studies of multi-site chemical exchange. I. Matrix formulation of the Bloch equations. Canadian Journal of Chemistry 1970;48(23):3641–3653.
67. Woessner DE, Zhang S, Merritt ME, Sherry AD. Numerical solution of the Bloch equations provides insights into the optimum design of PARACEST agents for MRI. Magn Reson Med 2005;53(4):790–799. [PubMed: 15799055]
68. Zhou J, Wilson DA, Sun PZ, Klaus JA, Van Zijl PC. Quantitative description of proton exchange processes between water and endogenous and exogenous agents for WEX, CEST, and APT experiments. Magn Reson Med 2004;51(5):945–952. [PubMed: 15122676]
69. Sun PZ, van Zijl PC, Zhou J. Optimization of the irradiation power in chemical exchange dependent saturation transfer experiments. J Magn Reson 2005;175(2):193–200. [PubMed: 15893487]
70. Ji Y, Zhou IY, Qiu BS, Sun PZ. Progress toward quantitative in vivo chemical exchange saturation transfer (CEST) MRI. Isr J Chem 2017;57(9):809–824.
71. Snoussi K, Bulte JW, Gueron M, van Zijl PC. Sensitive CEST agents based on nucleic acid imino proton exchange: detection of poly(rU) and of a dendrimer-poly(rU) model for nucleic acid delivery and pharmacology. Magn Reson Med 2003;49(6):998–1005. [PubMed: 12768576]
72. Baguet E, Roby C. Off-resonance irradiation effect in steady-state NMR saturation transfer. J Magn Reson 1997;128(2):149–160. [PubMed: 9356270]
73. Li AX, Hudson RH, Barrett JW, Jones CK, Pasternak SH, Bartha R. Four-pool modeling of proton exchange processes in biological systems in the presence of MRI-paramagnetic chemical exchange

saturation transfer (PARACEST) agents. Magn Reson Med 2008;60(5):1197–1206. [PubMed: 18958857]

74. Sun PZ, Longo DL, Hu W, Xiao G, Wu R. Quantification of iopamidol multi-site chemical exchange properties for ratiometric chemical exchange saturation transfer (CEST) imaging of pH. Phys Med Biol 2014;59(16):4493–4504. [PubMed: 25054859]
75. Sun PZ. Simplified and scalable numerical solution for describing multipool chemical exchange saturation transfer (CEST) MRI contrast. J Magn Reson 2010;205(2):235–241. [PubMed: 20570196]
76. Jin T, Wang P, Zong X, Kim SG. Magnetic resonance imaging of the Amine-Proton EXchange (APEX) dependent contrast. NeuroImage 2012;59(2):1218–1227. [PubMed: 21871570]
77. Zaiss M, Bachert P. Exchange-dependent relaxation in the rotating frame for slow and intermediate exchange -- modeling off-resonant spin-lock and chemical exchange saturation transfer. NMR Biomed 2013;26(5):507–518. [PubMed: 23281186]
78. Zaiss M, Bachert P. Chemical exchange saturation transfer (CEST) and MR Z-spectroscopy in vivo: a review of theoretical approaches and methods. Phys Med Biol 2013;58(22):R221–269. [PubMed: 24201125]
79. Jin T, Kim SG. Advantages of chemical exchange-sensitive spin-lock (CESL) over chemical exchange saturation transfer (CEST) for hydroxyl- and amine-water proton exchange studies. NMR Biomed 2014;27(11):1313–1324. [PubMed: 25199631]
80. Meissner JE, Goerke S, Rerich E, Klika KD, Radbruch A, Ladd ME, Bachert P, Zaiss M. Quantitative pulsed CEST-MRI using Omega-plots. NMR Biomed 2015;28(10):1196–1208. [PubMed: 26278686]
81. Roeloffs V, Meyer C, Bachert P, Zaiss M. Towards quantification of pulsed spinlock and CEST at clinical MR scanners: an analytical interleaved saturation-relaxation (ISAR) approach. NMR Biomed 2015;28(1):40–53. [PubMed: 25328046]
82. Gochberg DF, Does MD, Zu Z, Lankford CL. Towards an analytic solution for pulsed CEST. NMR Biomed 2018;31(5):e3903. [PubMed: 29460973]
83. Jiang W, Zhou IY, Wen L, Zhou X, Sun PZ. A theoretical analysis of chemical exchange saturation transfer echo planar imaging (CEST-EPI) steady state solution and the CEST sensitivity efficiency-based optimization approach. Contrast Media Mol Imaging 2016;11(5):415–423. [PubMed: 27312932]
84. Sun PZ. Quasi-steady state chemical exchange saturation transfer (QUASS CEST) analysis-correction of the finite relaxation delay and saturation time for robust CEST measurement. Magn Reson Med 2021;85(6):3281–3289. [PubMed: 33486816]
85. Zhou J, Payen JF, Wilson DA, Traystman RJ, van Zijl PC. Using the amide proton signals of intracellular proteins and peptides to detect pH effects in MRI. Nat Med 2003;9(8):1085–1090. [PubMed: 12872167]
86. Sun PZ, Wang E, Cheung JS, Zhang X, Benner T, Sorensen AG. Simulation and optimization of pulsed radio frequency (RF) irradiation scheme for chemical exchange saturation transfer (CEST) MRI – demonstration of pH-weighted pulsed-amide proton CEST MRI in an animal model of acute cerebral ischemia. Magnetic resonance in medicine 2011;66(4):1042–1048. [PubMed: 21437977]
87. Jin T, Wang P, Hitchens TK, Kim SG. Enhancing sensitivity of pH-weighted MRI with combination of amide and guanidyl CEST. NeuroImage 2017;157:341–350. [PubMed: 28602944]
88. Harris RJ, Cloughesy TF, Liau LM, Prins RM, Antonios JP, Li D, Yong WH, Pope WB, Lai A, Nghiemphu PL, Ellingson BM. pH-weighted molecular imaging of gliomas using amine chemical exchange saturation transfer MRI. Neuro Oncol 2015;17(11):1514–1524. [PubMed: 26113557]
89. Yao J, Tan CHP, Schlossman J, Chakhoyan A, Raymond C, Pope WB, Salamon N, Lai A, Ji M, Nghiemphu PL, Liau LM, Cloughesy TF, Ellingson BM. pH-weighted amine chemical exchange saturation transfer echoplanar imaging (CEST-EPI) as a potential early biomarker for bevacizumab failure in recurrent glioblastoma. J Neurooncol 2019;142(3):587–595. [PubMed: 30806888]
90. Harris RJ, Yao J, Chakhoyan A, Raymond C, Leu K, Liau LM, Nghiemphu PL, Lai A, Salamon N, Pope WB, Cloughesy TF, Ellingson BM. Simultaneous pH-sensitive and oxygen-sensitive MRI of human gliomas at 3 T using multi-echo amine proton chemical exchange saturation transfer spin-

and-gradient echo echo-planar imaging (CEST-SAGE-EPI). Magn Reson Med 2018;80(5):1962–1978. [PubMed: 29626359]

91. Wang YL, Yao J, Chakhoyan A, Raymond C, Salamon N, Liau LM, Nghiemphu PL, Lai A, Pope WB, Nguyen N, Ji M, Cloughesy TF, Ellingson BM. Association between Tumor Acidity and Hypervascularity in Human Gliomas Using pH-Weighted Amine Chemical Exchange Saturation Transfer Echo-Planar Imaging and Dynamic Susceptibility Contrast Perfusion MRI at 3T. AJNR Am J Neuroradiol 2019;40(6):979–986. [PubMed: 31097430]

92. Sun PZ, Benner T, Copen WA, Sorensen AG. Early experience of translating pH-weighted MRI to image human subjects at 3 Tesla. Stroke 2010;41(10 Suppl):S147–151. [PubMed: 20876492]

93. Jin T, Wang P, Zong X, Kim SG. MR imaging of the amide-proton transfer effect and the pH-insensitive nuclear overhauser effect at 9.4 T. Magn Reson Med 2013;69(3):760–770. [PubMed: 22577042]

94. Yuwen Zhou I, Wang E, Cheung JS, Lu D, Ji Y, Zhang X, Fulci G, Sun PZ. Direct saturation-corrected chemical exchange saturation transfer MRI of glioma: Simplified decoupling of amide proton transfer and nuclear overhauser effect contrasts. Magn Reson Med 2017;78(6):2307–2314. [PubMed: 29030880]

95. Wu Y, Chen Y, Zhao Y, Yang S, Zhao J, Zhou J, Chen Z, Sun PZ, Zheng H. Direct radiofrequency saturation corrected amide proton transfer tumor MRI at 3T. Magn Reson Med 2019;81(4):2710–2719. [PubMed: 30390326]

96. Sun PZ, Cheung JS, Wang E, Lo EH. Association between pH-weighted endogenous amide proton chemical exchange saturation transfer MRI and tissue lactic acidosis during acute ischemic stroke. J Cereb Blood Flow Metab 2011;31(8):1743–1750. [PubMed: 21386856]

97. Zaiss M, Xu J, Goerke S, Khan IS, Singer RJ, Gore JC, Gochberg DF, Bachert P. Inverse Z-spectrum analysis for spillover-, MT-, and T1 -corrected steady-state pulsed CEST-MRI--application to pH-weighted MRI of acute stroke. NMR Biomed 2014;27(3):240–252. [PubMed: 24395553]

98. Hua J, Jones CK, Blakeley J, Smith SA, van Zijl PC, Zhou J. Quantitative description of the asymmetry in magnetization transfer effects around the water resonance in the human brain. Magn Reson Med 2007;58(4):786–793. [PubMed: 17899597]

99. Jokivarsi KT, Grohn HI, Grohn OH, Kauppinen RA. Proton transfer ratio, lactate, and intracellular pH in acute cerebral ischemia. Magn Reson Med 2007;57(4):647–653. [PubMed: 17390356]

100. Liu D, Zhou J, Xue R, Zuo Z, An J, Wang DJ. Quantitative characterization of nuclear overhauser enhancement and amide proton transfer effects in the human brain at 7 tesla. Magn Reson Med 2013;70(4):1070–1081. [PubMed: 23238951]

101. Zhou J, Hong X, Zhao X, Gao JH, Yuan J. APT-weighted and NOE-weighted image contrasts in glioma with different RF saturation powers based on magnetization transfer ratio asymmetry analyses. Magn Reson Med 2013;70(2):320–327. [PubMed: 23661598]

102. Jones CK, Huang A, Xu J, Edden RA, Schar M, Hua J, Oskolkov N, Zaca D, Zhou J, McMahon MT, Pillai JJ, van Zijl PC. Nuclear Overhauser enhancement (NOE) imaging in the human brain at 7T. NeuroImage 2013;77(0):114–124. [PubMed: 23567889]

103. Li H, Zu Z, Zaiss M, Khan IS, Singer RJ, Gochberg DF, Bachert P, Gore JC, Xu J. Imaging of amide proton transfer and nuclear Overhauser enhancement in ischemic stroke with corrections for competing effects. NMR Biomed 2015;28(2):200–209. [PubMed: 25483870]

104. Zhou IY, Lu D, Ji Y, Wu L, Wang E, Cheung JS, Zhang XA, Sun PZ. Determination of multipool contributions to endogenous amide proton transfer effects in global ischemia with high spectral resolution in vivo chemical exchange saturation transfer MRI. Magn Reson Med 2019;81(1):645–652. [PubMed: 30058148]

105. Heo HY, Zhang Y, Burton TM, Jiang S, Zhao Y, van Zijl PCM, Leigh R, Zhou J. Improving the detection sensitivity of pH-weighted amide proton transfer MRI in acute stroke patients using extrapolated semisolid magnetization transfer reference signals. Magn Reson Med 2017;78(3):871–880. [PubMed: 28639301]

106. Wu Y, Zhou IY, Lu D, Manderville E, Lo EH, Zheng H, Sun PZ. pH-sensitive amide proton transfer effect dominates the magnetization transfer asymmetry contrast during acute

ischemia-quantification of multipool contribution to in vivo CEST MRI. Magn Reson Med 2018;79(3):1602–1608. [PubMed: 28733991]

107. Wu L, Jiang L, Sun PZ. Investigating the origin of pH-sensitive magnetization transfer ratio asymmetry MRI contrast during the acute stroke: Correction of T1 change reveals the dominant amide proton transfer MRI signal. Magnetic resonance in medicine 2020;84(5):2702–2712. [PubMed: 32416012]
108. Jokivarsi KT, Hiltunen Y, Grohn H, Tuunanen P, Grohn OH, Kauppinen RA. Estimation of the onset time of cerebral ischemia using T1rho and T2 MRI in rats. Stroke 2010;41(10):2335–2340. [PubMed: 20814006]
109. Guo Y, Zhou IY, Chan ST, Wang Y, Mandeville ET, Igarashi T, Lo EH, Ji X, Sun PZ. pH-sensitive MRI demarcates graded tissue acidification during acute stroke - pH specificity enhancement with magnetization transfer and relaxation-normalized amide proton transfer (APT) MRI. NeuroImage 2016;141:242–249. [PubMed: 27444569]
110. Zhu XH, Qiao H, Du F, Xiong Q, Liu X, Zhang X, Ugurbil K, Chen W. Quantitative imaging of energy expenditure in human brain. NeuroImage 2012;60(4):2107–2117. [PubMed: 22487547]
111. Henkelman RM, Stanisz GJ, Graham SJ. Magnetization transfer in MRI: a review. NMR Biomed 2001;14(2):57–64. [PubMed: 11320533]
112. Chang LH, Shirane R, Weinstein PR, James TL. Cerebral metabolite dynamics during temporary complete ischemia in rats monitored by time-shared 1H and 31P NMR spectroscopy. Magn Reson Med 1990;13(1):6–13. [PubMed: 2319935]
113. Sun PZ. Fast correction of B0 field inhomogeneity for pH-specific magnetization transfer and relaxation normalized amide proton transfer imaging of acute ischemic stroke without Z-spectrum. Magnetic resonance in medicine 2020;83(5):1688–1697. [PubMed: 31631414]
114. Sun PZ. Demonstration of magnetization transfer and relaxation normalized pH-specific pulse-amide proton transfer imaging in an animal model of acute stroke. Magnetic resonance in medicine 2020;84(3):1526–1533. [PubMed: 32080897]
115. Sun PZ. Consistent depiction of the acidic ischemic lesion with APT MRI-Dual RF power evaluation of pH-sensitive image in acute stroke. Magn Reson Med 2022;87(2):850–858. [PubMed: 34590730]
116. Sun PZ, Sorensen AG. Imaging pH using the chemical exchange saturation transfer (CEST) MRI: Correction of concomitant RF irradiation effects to quantify CEST MRI for chemical exchange rate and pH. Magn Reson Med 2008;60(2):390–397. [PubMed: 18666128]
117. Sun PZ. Simultaneous determination of labile proton concentration and exchange rate utilizing optimal RF power: Radio frequency power (RFP) dependence of chemical exchange saturation transfer (CEST) MRI. J Magn Reson 2010;202(2):155–161. [PubMed: 19926319]
118. McMahon MT, Gilad AA, Zhou J, Sun PZ, Bulte JW, van Zijl PC. Quantifying exchange rates in chemical exchange saturation transfer agents using the saturation time and saturation power dependencies of the magnetization transfer effect on the magnetic resonance imaging signal (QUEST and QUESP): Ph calibration for poly-L-lysine and a starburst dendrimer. Magn Reson Med 2006;55(4):836–847. [PubMed: 16506187]
119. Randtke EA, Chen LQ, Corrales LR, Pagel MD. The Hanes-Woolf linear QUESP method improves the measurements of fast chemical exchange rates with CEST MRI. Magn Reson Med 2014;71(4):1603–1612. [PubMed: 23780911]
120. Randtke EA, Chen LQ, Pagel MD. The reciprocal linear QUEST analysis method facilitates the measurements of chemical exchange rates with CEST MRI. Contrast Media Mol Imaging 2014;9(3):252–258. [PubMed: 24700753]
121. Sun PZ. Simplified quantification of labile proton concentration-weighted chemical exchange rate (kws) with RF saturation time dependent ratiometric analysis (QUESTRA): Normalization of relaxation and RF irradiation spillover effects for improved quantitative chemical exchange saturation transfer (CEST) MRI. Magnetic resonance in medicine 2012;67(4):936–942. [PubMed: 21842497]
122. Zaiss M, Angelovski G, Demetriou E, McMahon MT, Golay X, Scheffler K. QUESP and QUEST revisited - fast and accurate quantitative CEST experiments. Magn Reson Med 2018;79(3):1708–1721. [PubMed: 28686796]

123. Sun PZ, Wang Y, Xiao G, Wu R. Simultaneous experimental determination of labile proton fraction ratio and exchange rate with irradiation radio frequency power-dependent quantitative CEST MRI analysis. Contrast Media Mol Imaging 2013;8(3):246–251. [PubMed: 23606428]
124. Dixon WT, Ren J, Lubag AJ, Ratnakar J, Vinogradov E, Hancu I, Lenkinski RE, Sherry AD. A concentration-independent method to measure exchange rates in PARACEST agents. Magn Reson Med 2010;63(3):625–632. [PubMed: 20187174]
125. Sun PZ, Wang Y, Dai Z, Xiao G, Wu R. Quantitative chemical exchange saturation transfer (qCEST) MRI--RF spillover effect-corrected omega plot for simultaneous determination of labile proton fraction ratio and exchange rate. Contrast Media Mol Imaging 2014;9(4):268–275. [PubMed: 24706610]
126. Wu R, Xiao G, Zhou IY, Ran C, Sun PZ. Quantitative chemical exchange saturation transfer (qCEST) MRI - omega plot analysis of RF-spillover-corrected inverse CEST ratio asymmetry for simultaneous determination of labile proton ratio and exchange rate. NMR Biomed 2015;28(3):376–383. [PubMed: 25615718]
127. Rerich E, Zaiss M, Korzowski A, Ladd ME, Bachert P. Relaxation-compensated CEST-MRI at 7 T for mapping of creatine content and pH--preliminary application in human muscle tissue in vivo. NMR Biomed 2015;28(11):1402–1412. [PubMed: 26374674]
128. Shaghaghi M, Chen W, Scotti A, Ye H, Zhang Y, Zhu W, Cai K. In vivo quantification of proton exchange rate in healthy human brains with omega plot. Quant Imaging Med Surg 2019;9(10):1686–1696. [PubMed: 31728312]
129. Sun PZ. Quasi-steady-state CEST (QUASS CEST) solution improves the accuracy of CEST quantification: QUASS CEST MRI-based omega plot analysis. Magn Reson Med 2021;86(2):765–776. [PubMed: 33749052]
130. Sun PZ. Quasi-steady-state chemical exchange saturation transfer (QUASS CEST) MRI analysis enables T(1) normalized CEST quantification - Insight into T(1) contribution to CEST measurement. J Magn Reson 2021;329:107022. [PubMed: 34144360]
131. Kim H, Krishnamurthy LC, Sun PZ. Demonstration of fast multi-slice quasi-steady-state chemical exchange saturation transfer (QUASS CEST) human brain imaging at 3T. Magn Reson Med 2022;87(2):810–819. [PubMed: 34590726]
132. Zhang XY, Zhai Y, Jin Z, Li C, Sun PZ, Wu Y. Preliminary demonstration of in vivo quasi-steady-state CEST postprocessing-Correction of saturation time and relaxation delay for robust quantification of tumor MT and APT effects. Magn Reson Med 2021;86(2):943–953. [PubMed: 33723890]
133. Wu Y, Liu Z, Yang Q, Zou L, Zhang F, Qian L, Liu X, Zheng H, Luo D, Sun PZ. Fast and equilibrium CEST imaging of brain tumor patients at 3T. NeuroImage Clinical 2021;33:102890. [PubMed: 34864285]
134. Ji Y, Lu D, Jiang Y, Wang X, Meng Y, Sun PZ. Development of fast multi-slice apparent T1 mapping for improved arterial spin labeling MRI measurement of cerebral blood flow. Magn Reson Med 2021;85(3):1571–1580. [PubMed: 32970848]
135. Zhou IY, Fuss TL, Igarashi T, Jiang W, Zhou X, Cheng LL, Sun PZ. Tissue Characterization with Quantitative High-Resolution Magic Angle Spinning Chemical Exchange Saturation Transfer Z-Spectroscopy. Anal Chem 2016;88(21):10379–10383. [PubMed: 27709896]
136. Zhang XY, Wang F, Li H, Xu J, Gochberg DF, Gore JC, Zu Z. Accuracy in the quantification of chemical exchange saturation transfer (CEST) and relayed nuclear Overhauser enhancement (rNOE) saturation transfer effects. NMR Biomed 2017;30(7).
137. Zhang L, Martins AF, Mai Y, Zhao P, Funk AM, Clavijo Jordan MV, Zhang S, Chen W, Wu Y, Sherry AD. Imaging Extracellular Lactate In Vitro and In Vivo Using CEST MRI and a Paramagnetic Shift Reagent. Chemistry 2017;23(8):1752–1756. [PubMed: 27987233]
138. Zhou IY, Wang E, Cheung JS, Zhang X, Fulci G, Sun PZ. Quantitative chemical exchange saturation transfer (CEST) MRI of glioma using Image Downsampling Expedited Adaptive Least-squares (IDEAL) fitting. Sci Rep 2017;7(1):84. [PubMed: 28273886]
139. Zaiss M, Schmitt B, Bachert P. Quantitative separation of CEST effect from magnetization transfer and spillover effects by Lorentzian-line-fit analysis of z-spectra. J Magn Reson 2011;211(2):149–155. [PubMed: 21641247]

140. Zhang S, Seiler S, Wang X, Madhuranthakam AJ, Keupp J, Knippa EE, Lenkinski RE, Vinogradov E. CEST-Dixon for human breast lesion characterization at 3 T: A preliminary study. Magn Reson Med 2018;80(3):895–903. [PubMed: 29322559]
141. Heo HY, Zhang Y, Jiang S, Lee DH, Zhou J. Quantitative assessment of amide proton transfer (APT) and nuclear overhauser enhancement (NOE) imaging with extrapolated semisolid magnetization transfer reference (EMR) signals: II. Comparison of three EMR models and application to human brain glioma at 3 Tesla. Magn Reson Med 2016;75(4):1630–1639. [PubMed: 26033553]
142. Heo HY, Zhang Y, Lee DH, Hong X, Zhou J. Quantitative assessment of amide proton transfer (APT) and nuclear overhauser enhancement (NOE) imaging with extrapolated semi-solid magnetization transfer reference (EMR) signals: Application to a rat glioma model at 4.7 Tesla. Magn Reson Med 2016;75(1):137–149. [PubMed: 25753614]
143. Chung JJ, Jin T, Lee JH, Kim SG. Chemical exchange saturation transfer imaging of phosphocreatine in the muscle. Magn Reson Med 2019;81(6):3476–3487. [PubMed: 30687942]
144. Wu R, Liu CM, Liu PK, Sun PZ. Improved measurement of labile proton concentration-weighted chemical exchange rate (k(ws)) with experimental factor-compensated and T(1) -normalized quantitative chemical exchange saturation transfer (CEST) MRI. Contrast Media Mol Imaging 2012;7(4):384–389. [PubMed: 22649044]
145. Sun PZ, Wang E, Cheung JS. Imaging acute ischemic tissue acidosis with pH-sensitive endogenous amide proton transfer (APT) MRI--correction of tissue relaxation and concomitant RF irradiation effects toward mapping quantitative cerebral tissue pH. NeuroImage 2012;60(1):1–6. [PubMed: 22178815]
146. Zaiss M, Windschuh J, Paech D, Meissner JE, Burth S, Schmitt B, Kickingereder P, Wiestler B, Wick W, Bendszus M, Schlemmer HP, Ladd ME, Bachert P, Radbruch A. Relaxation-compensated CEST-MRI of the human brain at 7T: Unbiased insight into NOE and amide signal changes in human glioblastoma. NeuroImage 2015;112:180–188. [PubMed: 25727379]
147. Heo HY, Lee DH, Zhang Y, Zhao X, Jiang S, Chen M, Zhou J. Insight into the quantitative metrics of chemical exchange saturation transfer (CEST) imaging. Magn Reson Med 2017;77(5):1853–1865. [PubMed: 27170222]
148. Zu Z. Towards the complex dependence of MTRasym on T1w in amide proton transfer (APT) imaging. NMR Biomed 2018;31(7):e3934. [PubMed: 29806717]
149. Chappell MA, Donahue MJ, Tee YK, Khrapitchev AA, Sibson NR, Jezzard P, Payne SJ. Quantitative Bayesian model-based analysis of amide proton transfer MRI. Magn Reson Med 2013;70(2):556–567. [PubMed: 23008121]
150. Ray KJ, Larkin JR, Tee YK, Khrapitchev AA, Karunanithy G, Barber M, Baldwin AJ, Chappell MA, Sibson NR. Determination of an optimally sensitive and specific chemical exchange saturation transfer MRI quantification metric in relevant biological phantoms. NMR Biomed 2016;29(11):1624–1633. [PubMed: 27686882]
151. Tee YK, Harston GW, Blockley N, Okell TW, Levman J, Sheerin F, Cellerini M, Jezzard P, Kennedy J, Payne SJ, Chappell MA. Comparing different analysis methods for quantifying the MRI amide proton transfer (APT) effect in hyperacute stroke patients. NMR Biomed 2014;27(9):1019–1029. [PubMed: 24913989]
152. Msayib Y, Harston GWJ, Tee YK, Sheerin F, Blockley NP, Okell TW, Jezzard P, Kennedy J, Chappell MA. Quantitative CEST imaging of amide proton transfer in acute ischaemic stroke. Neuroimage Clin 2019;23:101833. [PubMed: 31063943]
153. Foo LS, Yap WS, Hum YC, Manan HA, Tee YK. Analysis of model-based and model-free CEST effect quantification methods for different medical applications. J Magn Reson 2020;310:106648. [PubMed: 31760147]
154. Ray KJ, Simard MA, Larkin JR, Coates J, Kinchesh P, Smart SC, Higgins GS, Chappell MA, Sibson NR. Tumor pH and Protein Concentration Contribute to the Signal of Amide Proton Transfer Magnetic Resonance Imaging. Cancer Res 2019;79(7):1343–1352. [PubMed: 30679178]
155. Aime S, Calabi L, Biondi L, De Miranda M, Ghelli S, Paleari L, Rebaudengo C, Terreno E. Iopamidol: Exploring the potential use of a well-established x-ray contrast agent for MRI. Magn Reson Med 2005;53(4):830–834. [PubMed: 15799043]

156. Longo DL, Dastru W, Digilio G, Keupp J, Langereis S, Lanzardo S, Prestigio S, Steinbach O, Terreno E, Uggeri F, Aime S. Iopamidol as a responsive MRI-chemical exchange saturation transfer contrast agent for pH mapping of kidneys: In vivo studies in mice at 7 T. Magn Reson Med 2011;65(1):202–211. [PubMed: 20949634]
157. Lindeman LR, Randtke EA, High RA, Jones KM, Howison CM, Pagel MD. A comparison of exogenous and endogenous CEST MRI methods for evaluating in vivo pH. Magn Reson Med 2018;79(5):2766–2772. [PubMed: 29024066]
158. Muller-Lutz A, Khalil N, Schmitt B, Jellus V, Pentang G, Oeltzschner G, Antoch G, Lanzman RS, Wittsack HJ. Pilot study of Iopamidol-based quantitative pH imaging on a clinical 3T MR scanner. Magma 2014;27(6):477–485. [PubMed: 24570337]
159. Chen Z, Han Z, Liu G. Repurposing Clinical Agents for Chemical Exchange Saturation Transfer Magnetic Resonance Imaging: Current Status and Future Perspectives. Pharmaceuticals (Basel, Switzerland) 2020;14(1).
160. Longo DL, Busato A, Lanzardo S, Antico F, Aime S. Imaging the pH evolution of an acute kidney injury model by means of iopamidol, a MRI-CEST pH-responsive contrast agent. Magn Reson Med 2013;70(3):859–864. [PubMed: 23059893]
161. Pavuluri K, Manoli I, Pass A, Li Y, Vernon HJ, Venditti CP, McMahon MT. Noninvasive monitoring of chronic kidney disease using pH and perfusion imaging. Science advances 2019;5(8):eaaw8357. [PubMed: 31453331]
162. Moon BF, Jones KM, Chen LQ, Liu P, Randtke EA, Howison CM, Pagel MD. A comparison of iopromide and iopamidol, two acidoCEST MRI contrast media that measure tumor extracellular pH. Contrast Media Mol Imaging 2015;10(6):446–455. [PubMed: 26108564]
163. Yang X, Song X, Ray Banerjee S, Li Y, Byun Y, Liu G, Bhujwalla ZM, Pomper MG, McMahon MT. Developing imidazoles as CEST MRI pH sensors. Contrast Media Mol Imaging 2016;11(4):304–312. [PubMed: 27071959]
164. Longo DL, Sun PZ, Consolino L, Michelotti FC, Uggeri F, Aime S. A general MRI-CEST ratiometric approach for pH imaging: demonstration of in vivo pH mapping with iobitridol. J Am Chem Soc 2014;136(41):14333–14336. [PubMed: 25238643]
165. Wu R, Longo DL, Aime S, Sun PZ. Quantitative description of radiofrequency (RF) power-based ratiometric chemical exchange saturation transfer (CEST) pH imaging. NMR Biomed 2015;28(5):555–565. [PubMed: 25807919]
166. Sun PZ, Xiao G, Zhou IY, Guo Y, Wu R. A method for accurate pH mapping with chemical exchange saturation transfer (CEST) MRI. Contrast Media Mol Imaging 2016;11(3):195–202. [PubMed: 26689424]
167. Wu Y, Zhou IY, Igarashi T, Longo DL, Aime S, Sun PZ. A generalized ratiometric chemical exchange saturation transfer (CEST) MRI approach for mapping renal pH using iopamidol. Magn Reson Med 2018;79(3):1553–1558. [PubMed: 28686805]
168. Zu Z, Janve VA, Li K, Does MD, Gore JC, Gochberg DF. Multi-angle ratiometric approach to measure chemical exchange in amide proton transfer imaging. Magn Reson Med 2012;68(3):711–719. [PubMed: 22161770]
169. McVicar N, Li AX, Goncalves DF, Bellyou M, Meakin SO, Prado MA, Bartha R. Quantitative tissue pH measurement during cerebral ischemia using amine and amide concentration-independent detection (AACID) with MRI. J Cereb Blood Flow Metab 2014;34(4):690–698. [PubMed: 24496171]
170. Chen M, Chen C, Shen Z, Zhang X, Chen Y, Lin F, Ma X, Zhuang C, Mao Y, Gan H, Chen P, Zong X, Wu R. Extracellular pH is a biomarker enabling detection of breast cancer and liver cancer using CEST MRI. Oncotarget 2017;8(28):45759–45767. [PubMed: 28501855]
171. Tang Y, Xiao G, Shen Z, Zhuang C, Xie Y, Zhang X, Yang Z, Guan J, Shen Y, Chen Y, Lai L, Chen Y, Chen S, Dai Z, Wang R, Wu R. Noninvasive Detection of Extracellular pH in Human Benign and Malignant Liver Tumors Using CEST MRI. Frontiers in oncology 2020;10:578985. [PubMed: 33224880]
172. Ceremuzynski L, Budaj A, Czepiel A, Burzykowski T, Achremczyk P, Smielak-Korombel W, Maciejewicz J, Dziubinska J, Nartowicz E, Kawka-Urbanek T, Piotrowski W, Hanzlik J, Cieslinski A, Kawecka-Jaszcz K, Gessek J, Wrabec K. Low-dose glucose-insulin-potassium is

ineffective in acute myocardial infarction: results of a randomized multicenter Pol-GIK trial. Cardiovasc Drugs Ther 1999;13(3):191–200. [PubMed: 10439881]

173. Raghunand N, Howison C, Sherry AD, Zhang S, Gillies RJ. Renal and systemic pH imaging by contrast-enhanced MRI. Magn Reson Med 2003;49(2):249–257. [PubMed: 12541244]
174. Garcia-Martin ML, Martinez GV, Raghunand N, Sherry AD, Zhang S, Gillies RJ. High resolution pH(e) imaging of rat glioma using pH-dependent relaxivity. Magn Reson Med 2006;55(2):309–315. [PubMed: 16402385]
175. Martinez GV, Zhang X, Garcia-Martin ML, Morse DL, Woods M, Sherry AD, Gillies RJ. Imaging the extracellular pH of tumors by MRI after injection of a single cocktail of T1 and T2 contrast agents. NMR Biomed 2011;24(10):1380–1391. [PubMed: 21604311]
176. Coman D, Huang Y, Rao JU, De Feyter HM, Rothman DL, Juchem C, Hyder F. Imaging the intratumoral-peritumoral extracellular pH gradient of gliomas. NMR Biomed 2016;29(3):309–319. [PubMed: 26752688]
177. Rao JU, Coman D, Walsh JJ, Ali MM, Huang Y, Hyder F. Temozolomide arrests glioma growth and normalizes intratumoral extracellular pH. Sci Rep 2017;7(1):7865. [PubMed: 28801587]
178. Coman D, Peters DC, Walsh JJ, Savic LJ, Huber S, Sinusas AJ, Lin M, Chapiro J, Constable RT, Rothman DL, Duncan JS, Hyder F. Extracellular pH mapping of liver cancer on a clinical 3T MRI scanner. Magn Reson Med 2020;83(5):1553–1564. [PubMed: 31691371]
179. Shah T, Lu L, Dell KM, Pagel MD, Griswold MA, Flask CA. CEST-FISP: a novel technique for rapid chemical exchange saturation transfer MRI at 7 T. Magn Reson Med 2011;65(2):432–437. [PubMed: 20939092]
180. Sun PZ, Benner T, Kumar A, Sorensen AG. Investigation of optimizing and translating pH-sensitive pulsed-chemical exchange saturation transfer (CEST) imaging to a 3T clinical scanner. Magn Reson Med 2008;60(4):834–841. [PubMed: 18816867]
181. Zu Z, Li K, Janve VA, Does MD, Gochberg DF. Optimizing pulsed-chemical exchange saturation transfer imaging sequences. Magn Reson Med 2011;66(4):1100–1108. [PubMed: 21432903]
182. Xiao G, Sun PZ, Wu R. Fast simulation and optimization of pulse-train chemical exchange saturation transfer (CEST) imaging. Phys Med Biol 2015;60(12):4719–4730. [PubMed: 26020414]
183. Zu Z, Xu J, Li H, Chekmenev EY, Quarles CC, Does MD, Gore JC, Gochberg DF. Imaging amide proton transfer and nuclear overhauser enhancement using chemical exchange rotation transfer (CERT). Magn Reson Med 2014;72(2):471–476. [PubMed: 24302497]
184. Zu Z, Louie EA, Lin EC, Jiang X, Does MD, Gore JC, Gochberg DF. Chemical exchange rotation transfer imaging of intermediate-exchanging amines at 2 ppm. NMR Biomed 2017;30(10):e3756.
185. Sun PZ, Murata Y, Lu J, Wang X, Lo EH, Sorensen AG. Relaxation-compensated fast multislice amide proton transfer (APT) imaging of acute ischemic stroke. Magn Reson Med 2008;59(5):1175–1182. [PubMed: 18429031]
186. Sun PZ, Cheung JS, Wang E, Benner T, Sorensen AG. Fast multislice pH-weighted chemical exchange saturation transfer (CEST) MRI with Unevenly segmented RF irradiation. Magn Reson Med 2011;65(2):588–594. [PubMed: 20872859]
187. Villano D, Romdhane F, Irrera P, Consolino L, Anemone A, Zaiss M, Dastru W, Longo DL. A fast multislice sequence for 3D MRI-CEST pH imaging. Magn Reson Med 2021;85(3):1335–1349. [PubMed: 33031591]
188. Zhu H, Jones CK, van Zijl PC, Barker PB, Zhou J. Fast 3D chemical exchange saturation transfer (CEST) imaging of the human brain. Magn Reson Med 2010;64(3):638–644. [PubMed: 20632402]
189. Jones CK, Polders D, Hua J, Zhu H, Hoogduin HJ, Zhou J, Luijten P, van Zijl PC. In vivo three-dimensional whole-brain pulsed steady-state chemical exchange saturation transfer at 7 T. Magn Reson Med 2012;67(6):1579–1589. [PubMed: 22083645]
190. Akbey S, Ehses P, Stirnberg R, Zaiss M, Stocker T. Whole-brain snapshot CEST imaging at 7 T using 3D-EPI. Magn Reson Med 2019;82(5):1741–1752. [PubMed: 31199016]
191. Demetriou E, Kujawa A, Golay X. Pulse sequences for measuring exchange rates between proton species: From unlocalised NMR spectroscopy to chemical exchange saturation transfer imaging. Progress in nuclear magnetic resonance spectroscopy 2020;120-121:25–71. [PubMed: 33198968]

192. Sun PZ, Farrar CT, Sorensen AG. Correction for artifacts induced by B(0) and B(1) field inhomogeneities in pH-sensitive chemical exchange saturation transfer (CEST) imaging. Magn Reson Med 2007;58(6):1207–1215. [PubMed: 17969015]

193. Kim M, Gillen J, Landman BA, Zhou J, van Zijl PC. Water saturation shift referencing (WASSR) for chemical exchange saturation transfer (CEST) experiments. Magn Reson Med 2009;61(6):1441–1450. [PubMed: 19358232]

194. Singh A, Haris M, Cai K, Kassey VB, Kogan F, Reddy D, Hariharan H, Reddy R. Chemical exchange saturation transfer magnetic resonance imaging of human knee cartilage at 3 T and 7 T. Magn Reson Med 2012;68(2):588–594. [PubMed: 22213239]

195. Wei W, Jia G, Flanigan D, Zhou J, Knopp MV. Chemical exchange saturation transfer MR imaging of articular cartilage glycosaminoglycans at 3 T: Accuracy of B0 Field Inhomogeneity corrections with gradient echo method. Magn Reson Imaging 2014;32(1):41–47. [PubMed: 24119460]

196. Li Y, Xie D, Cember A, Nanga RPR, Yang H, Kumar D, Hariharan H, Bai L, Detre JA, Reddy R, Wang Z. Accelerating GluCEST imaging using deep learning for B0 correction. Magn Reson Med 2020;84(4):1724–1733. [PubMed: 32301185]

197. Sun PZ. Development of intravoxel inhomogeneity correction for chemical exchange saturation transfer (CEST) spectral imaging – A high-resolution field map-based deconvolution algorithm for magnetic field inhomogeneity correction Magnetic resonance in medicine 2020;83(4):1348–1355. [PubMed: 31628765]

198. Schuenke P, Windschuh J, Roeloffs V, Ladd ME, Bachert P, Zaiss M. Simultaneous mapping of water shift and B1 (WASABI)-Application to field-Inhomogeneity correction of CEST MRI data. Magn Reson Med 2017;77(2):571–580. [PubMed: 26857219]

199. Sun PZ, Lu J, Wu Y, Xiao G, Wu R. Evaluation of the dependence of CEST-EPI measurement on repetition time, RF irradiation duty cycle and imaging flip angle for enhanced pH sensitivity. Phys Med Biol 2013;58(17):N229–240. [PubMed: 23939228]

200. Zhou J, Blakeley JO, Hua J, Kim M, Laterra J, Pomper MG, van Zijl PC. Practical data acquisition method for human brain tumor amide proton transfer (APT) imaging. Magn Reson Med 2008;60(4):842–849. [PubMed: 18816868]

201. Tee YK, Khrapitchev AA, Sibson NR, Payne SJ, Chappell MA. Optimal sampling schedule for chemical exchange saturation transfer. Magn Reson Med 2013;70(5):1251–1262. [PubMed: 23315799]

202. Yang S, Wu Y. Investigation of the performance of variable-density Z-spectrum acquisition scheme in MR chemical exchange saturation transfer effect quantification. Engineering in Medicine and Biology Society (EMBC), 2013 35th Annual International Conference of the IEEE 2015;2015:7929–7932.

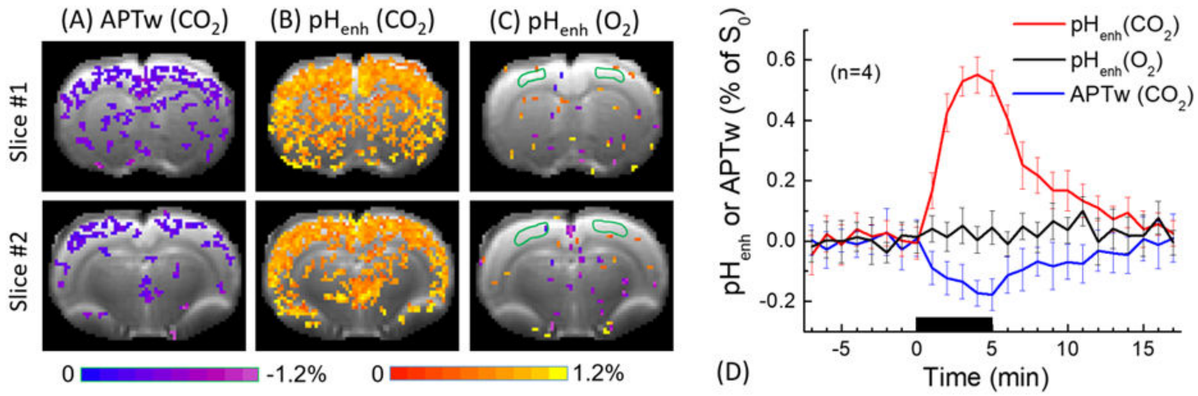

Fig. 1.

Comparison of pH-weighted APTw and pH_{enh} following hypercapnic and hyperoxia challenges. a) Signal change in APTw map following hypercapnia. b) Signal change in pH_{enh} map following hypercapnia. c) pH_{enh} MRI signal change following hyperoxia. d) The timecourse of APTw and pH_{enh} following hypercapnic and hyperoxia challenges (Jin et al. Neuroimage 2017;157:341-350.)

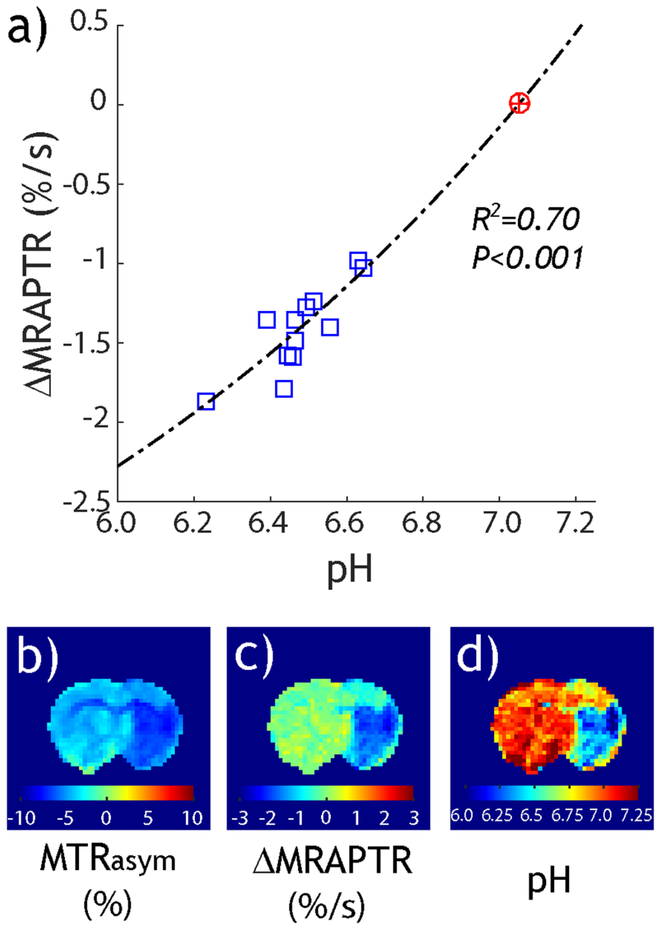

Fig. 2.

Tissue pH MRI from pH-specific MRAPT analysis. a) The pH-specific ΔMRAPTR and pH are highly correlated. b) pH-weighted MTR$_{asym}$ map. c) pH-specific ΔMRAPTR map. d) Tissue pH image derived from ΔMRAPTR image and its pH calibration (Wang et al. Neuroimage 2019;191:610-7.)

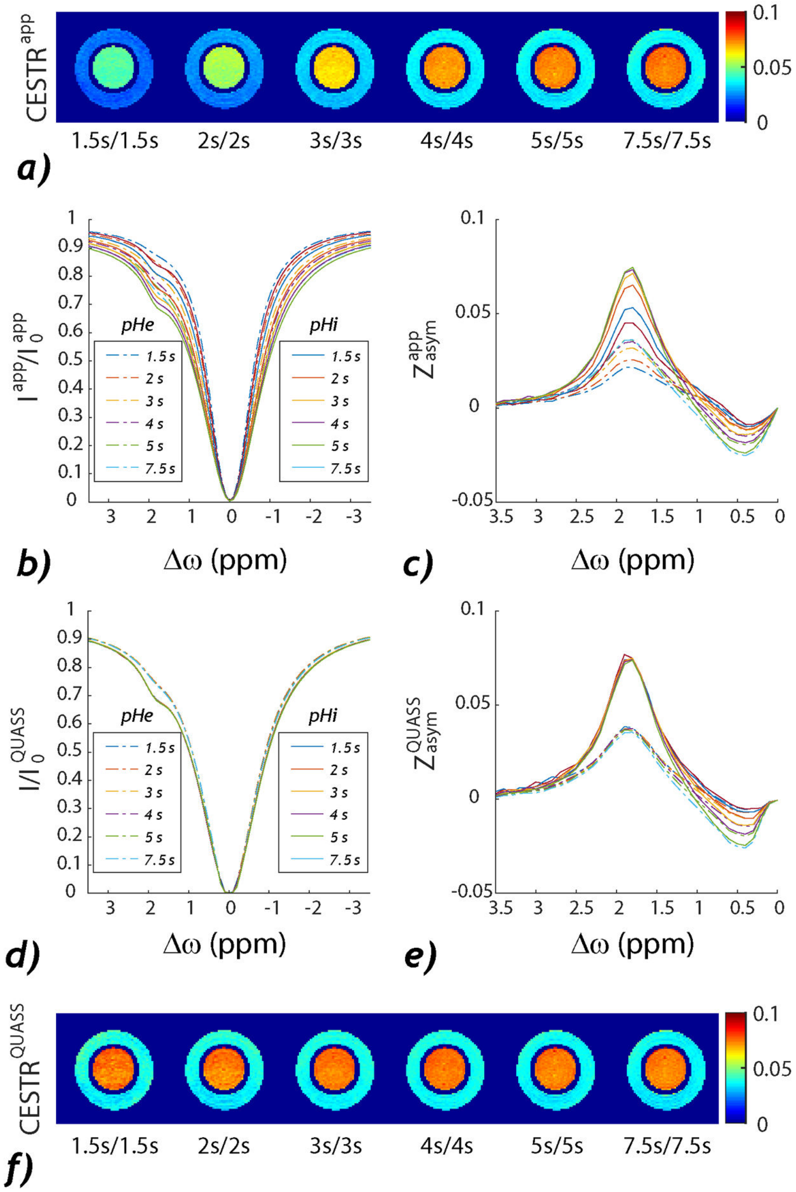

Fig. 3.

Comparison of the conventional and QUASS CEST MRI from a creatine pH phantom.

a) Routine MTR_{asym} at 1.9 ppm obtained under different Td and Ts. b) Z-spectra and c) asymmetry spectra. d) The corresponding QUASS Z-spectra and d) QUASS asymmetry spectra. e) The QUASS MTR_{asym} at 1.9 ppm under different Td and Ts. (Sun. Magn Reson Med 2021;86(2):765-776.)

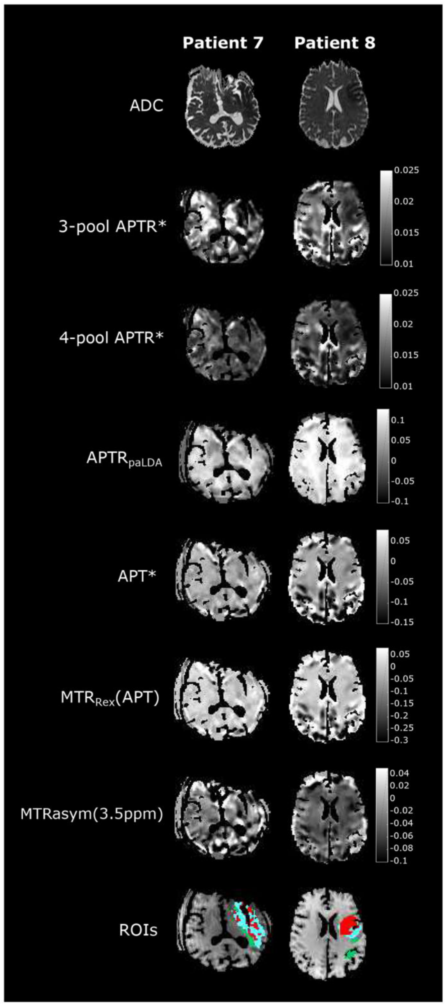

Fig. 4.

Comparison of different CEST indices in acute stroke patient imaging. The model-based Bayesian CEST images capture pH drop in the ischemic lesion with the least spatial variability (Msayib et al., NeuroImage: Clinical 2019;23:101833.)

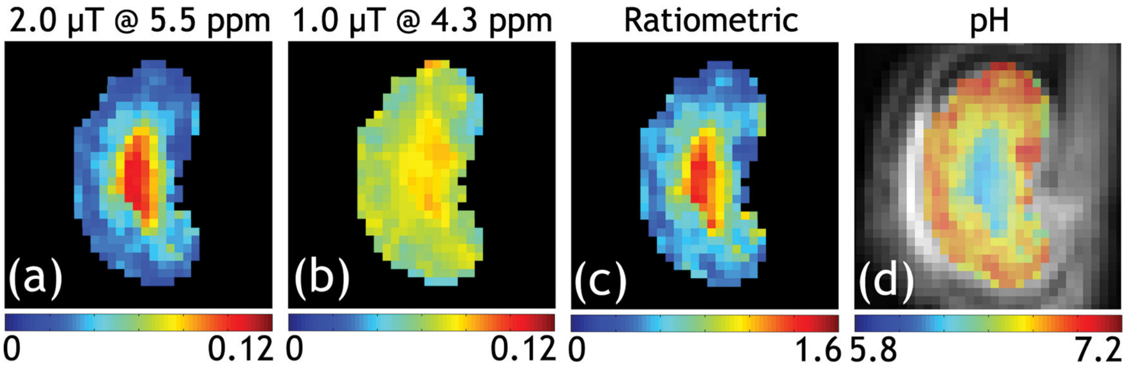

Fig. 5.

A representative normal kidney pH map from the generalized ratiometric pH imaging at 4.7 T. The iopamidol CEST effects were measured with two RF amplitudes, and the peaks were isolated for 4.3 ppm (1 μT) and 5.5 ppm (2 μT). Their ratio map is pH-dependent, which permits absolute pH mapping (Wu et al. Magnetic Resonance in Medicine, 2018;79:1553-58.)

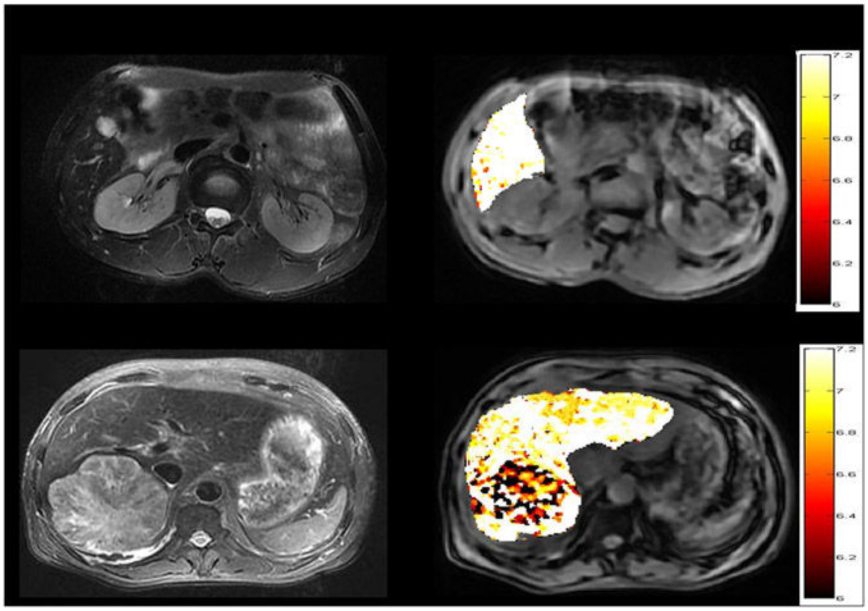

Fig. 6.

Liver pH imaging with CEST MRI of Ioversol. a) A structural image of a hepatic hemangioma patient. b) pH map shows consistent pHe with the surrounding normal tissue. c) A structural image of a hepatic carcinoma patient. d) Tumor pH map is noticeably lower than normal tissue (Tang et al. Frontiers in oncology 2020;10:578985.)